Review

Xuhan Guo, Xingchen Ji, Baicheng Yao, Teng Tan, Allen Chu, Ohad Westreich, Avik Dutt*, Cheewei Wong* and Yikai Su*

Ultra-wideband integrated photonic devices on silicon platform: from visible to mid-IR

https://doi.org/10.1515/nanoph-2022-0575
Received September 21, 2022; accepted January 2, 2023; published online January 18, 2023

Abstract: Silicon photonics has gained great success mainly due to the promise of realizing compact devices in high volume through the low-cost foundry model. It is burgeoning from laboratory research into commercial production endeavors such as datacom and telecom. However, it is unsuitable for some emerging applications which require coverage across the visible or mid infrared (mid-IR) wavelength bands. It is desirable to introduce other wideband materials through heterogeneous integration, while keeping the integration compatible with wafer-scale fabrication processes on silicon substrates. We discuss the properties of silicon-family materials including silicon, silicon nitride, and silica, and other non-group IV materials such as metal oxide, tantalum pentoxide, lithium niobate, aluminum nitride, gallium nitride, barium titanate, piezoelectric lead zirconate titanate, and 2D materials. Typical examples of devices using these materials on silicon platform are provided. We then introduce a general fabrication method and low-loss process treatment for photonic devices on the silicon platform. From an applications viewpoint, we focus on three new areas requiring integration: sensing, optical comb generation, and quantum information processing. Finally, we conclude with perspectives on how new materials and integration methods can address previously unattainable wavelength bands while maintaining the advantages of silicon, thus showing great potential for future widespread applications.

Keywords: heterogeneous integration; mid infrared; silicon photonics; visible; wide bandgap.

1 Introduction

Silicon photonics has gained great success in many areas owing to the high-density feature and compatibility with complementary metal-oxide-semiconductor (CMOS) fabrication technique where low cost is necessary, starting from telecom application as a representative example in the 1.5-μm wavelength band. However, the transparency window of silicon is from 1.1 μm to 8.5 μm due to its material bandgap, and hence, silicon is unsuitable for some emerging applications which require visible or mid infrared (mid-IR) wavelengths, such as quantum optics [1, 2], precision metrology and spectroscopy [3, 4], red–green–blue (RGB) displays [5], atomic clocks [6], computing [7, 8], remote sensing [9], etc.

It is very challenging for a single-material system to offer solutions to diverse application requirements spanning from the visible to the mid-IR. Wide bandgap photonic circuits may rely on heterogeneous integration of multiple material systems, while the integration is desired to be compatible with wafer-scale fabrication processes starting from silicon substrates. Incorporation of new materials with silicon is possible either with alternative moderate-index-contrast systems that are manufacturable in the same CMOS environment (Silica, Si_3N_4, etc.) or through

***Corresponding authors: Avik Dutt**, Mechanical Engineering, and Institute for Physical Science and Technology, University of Maryland, College Park, USA, E-mail: avikdutt@umd.edu; **Cheewei Wong**, Fang Lu Mesoscopic Optics and Quantum Electronics Laboratory, University of California, Los Angeles, CA, USA, E-mail: cheewei.wong@ucla.edu; and **Yikai Su**, State Key Laboratory of Advanced Optical Communication Systems and Networks, Shanghai Jiao Tong University, Shanghai, China, E-mail: yikaisu@sjtu.edu.cn. https://orcid.org/0000-0002-1526-8187 (Y. Su)
Xuhan Guo, State Key Laboratory of Advanced Optical Communication Systems and Networks, Shanghai Jiao Tong University, Shanghai, China. https://orcid.org/0000-0002-4891-0201
Xingchen Ji, John Hopcroft Center for Computer Science, School of Electronic Information and Electrical Engineering, Shanghai Jiao Tong University, Shanghai 200240, China
Baicheng Yao and Teng Tan, Key Laboratory of Optical Fibre Sensing and Communications (Education Ministry of China), University of Electronic Science and Technology of China, Chengdu, China
Allen Chu, Fang Lu Mesoscopic Optics and Quantum Electronics Laboratory, University of California, Los Angeles, CA, USA
Ohad Westreich, Applied Physics Division, Soreq NRC, Yavne 81800, Israel

heterogeneous integration with other wide bandgap materials (LN, Ta_2O_2, Al_2O_3, AIN, 2D materials, etc.). These methods can reach the previously unattainable wavelength bands by using wide band gap semiconductors, while maintaining the advantages of silicon, thus showing great potential for future research and applications. Some other wide bandgap materials are also drawing great attentions. For example, the chalcogenide glass that replaces oxygen with heavier chalcogens is one of wide bandgap semiconductor optical materials [10], which exhibits broadband transparency, high and continuously tunable refractive indices (n ~2–3.5) and large Kerr nonlinearity (~10^{-18} m^2 W^{-1}). Hybrid silicon-chalcogenide glass photonic integrated circuits [11] as well as photonic integration of 2D materials using chalcogenide glass [12] have been demonstrated. Germanium (Ge) is also a promising mid-IR optical material with high refractive index ($n = 4.0$) and a large transparency range up to 14.6 μm [13]. Due to the page limit, chalcogenide glass and Ge materials on silicon are not covered in this review.

In this paper, we review the latest development of ultra-wideband integrated photonic devices based on the silicon platform from visible to mid-IR, including material properties, fabrication, structures and applications, so as to illustrate the development towards new applications. The review paper is organized as follows: Firstly, we will start with wideband materials and integrated photonic devices on the silicon platform, including their optical properties, representative structures, general fabrication process and the latest research progress of the functional wideband components. Secondly, we will focus on the emerging applications from the perspective of different operating wavelength bands. Finally, we will discuss the challenges toward realization of ultra-wideband integrated systems, motivating the need for wide bandgap integrated photonic devices. We hope to address the latest advances in these wideband silicon-based devices and provide some vision for the future of next-generation integrated photonics.

2 Materials and integrated photonic devices on silicon platform

Benefiting from the scaling of mature CMOS-compatible foundries and the associated toolkits first developed for the microelectronics ecosystem, silicon photonics has been thriving from laboratory research and development (R & D) into commercial production endeavors such as datacom and telecom, where high-volume and low-cost foundry models are critical. Silicon-on-isolator (SOI) is undoubtedly the leading material platform, which has successfully realized various high-performance components and characteristic applications, mainly in a spectral range of 1.1–3.8 μm, where both silicon and silica are transparent [14], especially near the communication windows of 1.31 (O-band) and 1.55 μm (C-band) [15].

The range of transparency determines the potential application fields of a material platform. Recently, a wide range of emerging applications have driven the need for new wide-bandwidth photonic integration other than telecom and datacom, as illustrated in Figure 1, which require low optical losses extending from the visible (~400 nm–700 nm) to the mid-infrared (mid-IR, ~20 μm). For instance, mid-IR is a very important wave band for photonics which encompasses multiple atmospheric sensing windows covering the fingerprint region (7–20 μm) as well as the primary absorption peaks/bands of typical chemical and biological molecules [16], including CO_2 (2.65 μm, 4.2–4.3 μm), CH_4 (3.2–3.45 μm) and CO (~4.5 μm), etc., and some other toxic gases such as HF (2.33–2.78 μm) and H_2S (2.5–2.75 μm) etc. These windows are of huge interest to spectroscopic sensing, thermal imaging and infrared homing, etc.

These new applications require different on-chip properties within the wavelength range of interest, either low linear loss for the passive components (i.e. waveguides, splitters, filters, and demultiplexers), or the nonlinearity and dispersion properties (i.e. electro-optic, optoelectronic, and thermo–optic) for active components (i.e. modulators, phase shifters, photodiodes, and comb generators), or piezoelectric property (i.e. microelectromechanical systems (MEMS)). However, application spaces for silicon photonics in these wavelength ranges are still immature, mainly limited by the nontransparent wavelength window, or high waveguide loss, or the inefficient nonlinearity for high power handling. Therefore, in order to expand the operating wavelength ranges and applications, there is an increasing trend in scaling up silicon-based devices [17]. To realize the ultra-wideband applications and leverage the successful silicon photonic integrated circuits technologies, the wideband integrated photonic devices on silicon platform will most likely support heterogeneous integration of a range of passive and active functionalities, as well as the ability to enable low loss components and high integration density, the realization of high-performance passive, active and nonlinear components, and some unique material properties to realize novel devices. Various wide bandgap semiconductor optical materials with low losses have beenr

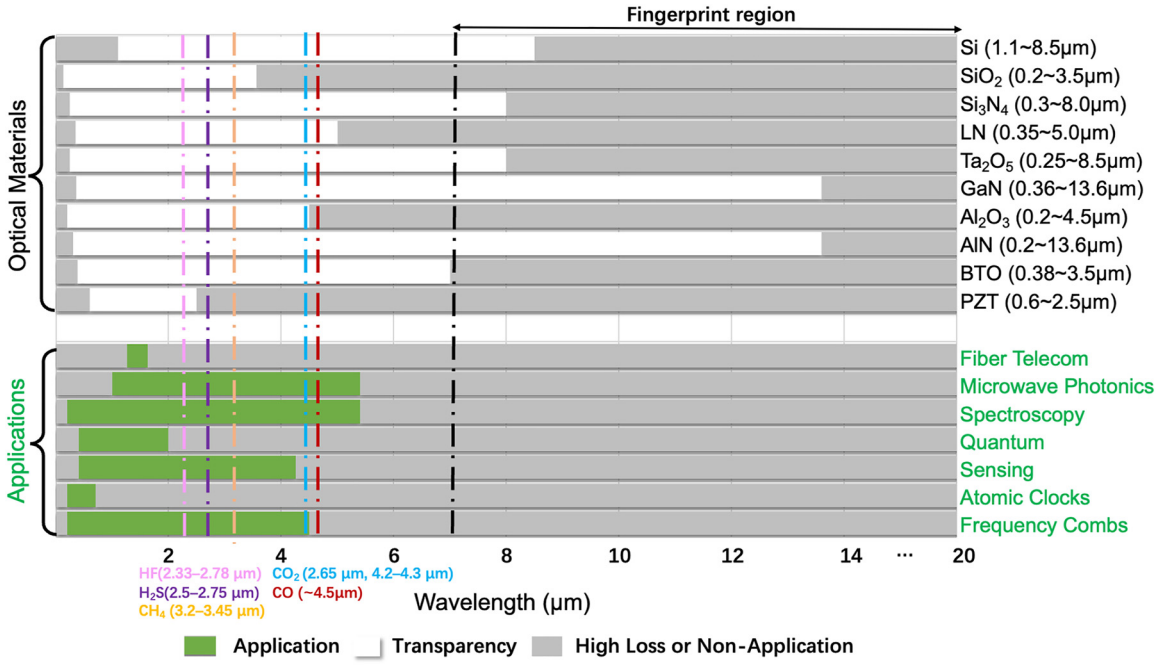

Figure 1: Transparency windows of different photonic materials and applications over various spectral windows.

demonstrated that can support wafer-scale o heterogeneous integration, of which the most reported materials include silicon family materials such as silica (SiO_2) and silicon nitride (Si_3N_4), or the promising wideband optical material that can be integrated on silicon platform through various integration approaches, i.e. 2D materials, aluminum nitride (AlN), gallium nitride (GaN), aluminum oxide (Al_2O_3), tantalum pentoxide (Ta_2O_3), lithium niobate (LN), barium titanate ($BaTiO_3$–BTO), and lead zirconate titanate (PZT).

The typical transparency windows of different photonic materials and applications over various spectral windows are shown in Figure 1.

2.1 Silicon-family materials

Silicon-family materials based on mature silicon photonic platforms mainly include silicon, silicon nitride, and silica. As silicon's crystal structure has inversion symmetry (hence classified as "centro-symmetric" without the second order nonlinear response (Pockels effect)), the silicon-family materials do not show the linear electro-optic (EO) effect when an electric field is applied. Most silicon-family material and related application fields focus on their superior passive performances [15]. The optical properties of the silicon family are summarized in Table 1.

Table 1: Optical properties of the silicon family [14, 15, 18].

Parameter	Si	Si_3N_4	SiO_2
Bandgap	1.14 eV (1.09 μm)	5.0 eV (0.25 μm)	9.3 eV (0.13 μm)
Refractive index at 1.55 μm	3.487	~2.0	1.444
TO coefficient (K^{-1})	1.86×10^{-4}	2.45×10^{-5}	0.95×10^{-5}
TPA coefficient	9×10^{-12}	0	–
Kerr coefficient (m^2W^{-1})	4.4×10^{-18}	2.4×10^{-19} [19]	2.2×10^{-20} [20]
Typical waveguide loss around 1.55 μm (dB/cm)	1 ~ 1.5	0.001 ~ 0.5	<0.1
Cladding	Silica/air	Silica	Air
Pockels effect	–	–	–

2.1.1 Silicon

Silicon exhibits a very high refractive index of ∼3.4, making it possible to realize compact footprint and densely-integrated devices on a commercial SOI wafer. Silicon material itself shows low absorption in the wavelength range of 1.1–8.5 μm, which covers the near-infrared (near-IR) and mid-infrared (mid-IR) regions. However, the prevailing SOI platform for silicon photonics is mainly transparent between 1.1 μm and 4 μm [14]. Below 1.1 μm, silicon strongly absorbs the guiding light, and its lower limit is determined by the narrow bandgap, but it can be used for photodetection. Beyond ∼4 μm, for silicon devices with buried oxide (BOX) or cladding layer, there is a sharp onset of mid-IR absorption of the in the range of 2.6∼2.9 μm and beyond 3.6 μm [21]. Some typical devices of silicon are shown in Figure 2(a) with two examples: a silicon nanobeam filter with an ultrahigh thermo-optic tuning efficiency of 21 nm/mW over a wide continuous tuning range of ∼43.9 nm [22], a micrometer-scale silicon electro-optic modulator with a modulation speed of 1.5 Gbit/s [23] and an on-chip optical delay line based on silicon waveguides and cascaded microring resonators with group delays exceeding 500 ps and a footprint less than 0.09 mm^2 [24].

Due to the fabrication compatibility with CMOS pilot lines and good optical properties, silicon photonics based

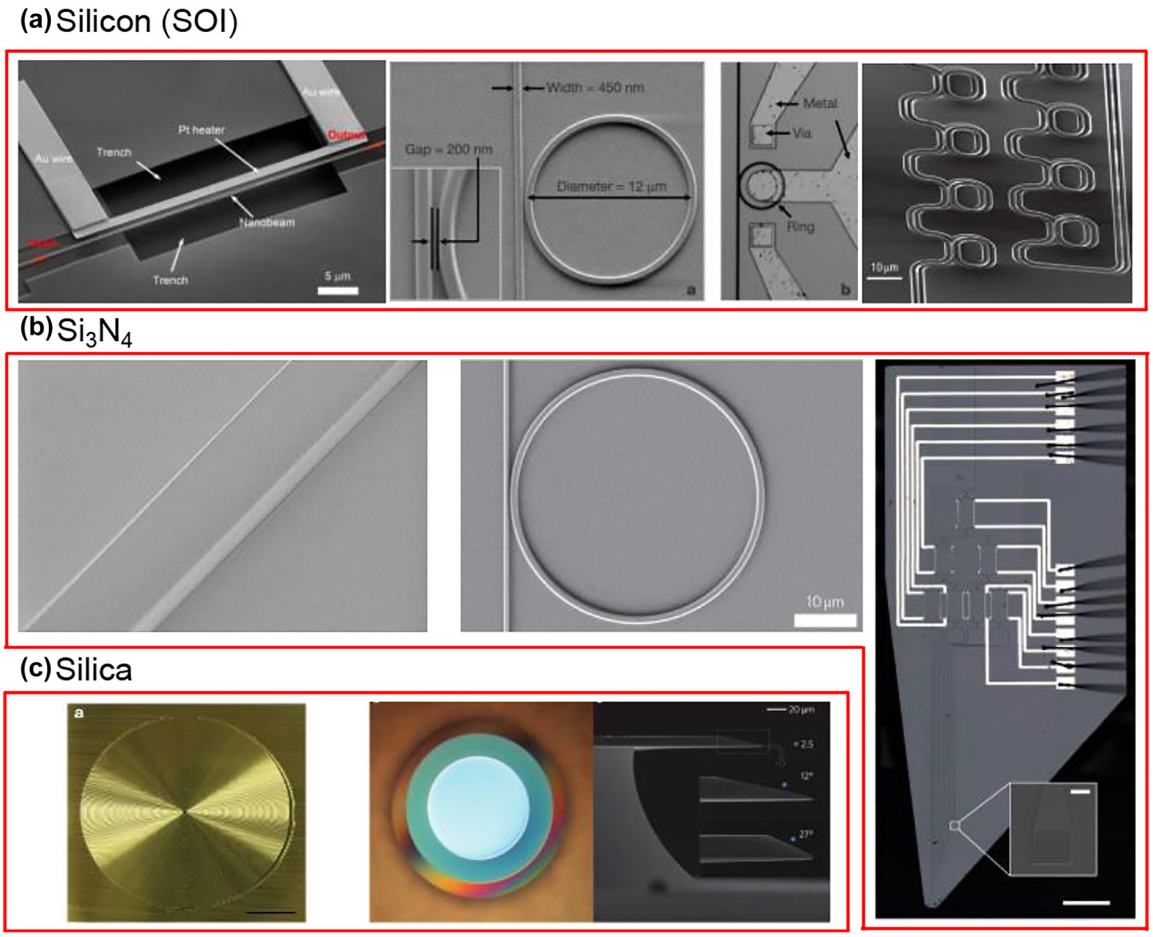

Figure 2: Typical devices of silicon-family materials. (a) Silicon: a single-resonance silicon nanobeam filter [22]; a micrometer-scale silicon electro-optic modulator [23]; an on-chip silicon waveguides and cascaded microring resonators based optical delay line [24]. (b) Silicon nitride: scanning electron microscopy (SEM) image of a fabricated silicon nitride waveguide [50]; a SEM of a silicon nitride optical parametric oscillator [51]; a silicon nitride switch [52]. (c) Silica: a silica spiral delay line [87]; micrographs and SEM of a chemically etched ultrahigh-Q wedge-resonator on a silicon chip [88]. [(a) Reproduced with permission from reference [22]. Copyright © 2018, optical society of America; reproduced with permission from reference [23]. Copyright © 2005, nature publishing group; reproduced with permission from reference [24]. Copyright © 2005, nature publishing group; (b) reproduced with permission from reference [50]. Copyright © 2017, optical society of America; reproduced with permission from reference [51]. Copyright © 2009, nature publishing group; reproduced with permission from reference [52]. Copyright © 2020, nature publishing group; (c) reproduced with permission from reference [87]. Copyright © 2012, nature publishing group; reproduced with permission from reference [88]. Copyright © 2012, nature publishing group].

on SOI platform has predominantly been used to demonstrate components for short and long haul communication systems in near-IR range (1.26∼1.63 μm). Fully etched silicon strip waveguides have a typical waveguide loss of ∼1.5 dB/cm for TE polarized light in the C-band, and the loss can be further reduced to ∼0.7 dB/cm for partially etched rib waveguides [25]. Amongst other functional components [25, 26] include various high-speed transceivers [27], modulators [28], wavelength filters for wavelength division multiplexing (WDM) systems [29] and photodetectors [30]. Starting from the great success in telecommunications, other applications such as optical spectrometers [31], optical neural networks [32, 33], and nonlinear applications [34] have also been demonstrated. Vast reviews of silicon photonic devices and applications in the near-IR band can be found in [15, 25, 35]. Silicon has a large third-order non-linearity with a large Kerr index (4.4×10^{-18} m^2 W^{-1}), however, the presence of two-photon absorption (TPA) resulting from its small bandgap of 1.1 eV and induced free-carrier absorption make it inefficient for nonlinear applications or other high power handling applications [25] in the telecommunication band. Silicon is also very sensitive to temperature variations due to the high thermo−optic (TO) coefficient of 1.86×10^{-4} K^{-1}. This TO effect has been utilized for implementing tunable filters, low-speed thermo-optic switches, couplers with arbitrary coupling ratios or to compensate fabrication-induced phase errors on delay lines or wavelength sensitive filters.

For wavelengths beyond ∼2.2 μm (i.e. twice the bandgap wavelength of 1.1 μm), there is a set of gases characteristic absorption peaks in this band [16]. TPA problem in silicon is also drastically reduced, making silicon waveguide structures ideal for implementing new scenarios, such as spectroscopic, sensing applications, and nonlinear optical devices in the mid-IR [36–38]. In order to fully utilize the wavelength transparency window of silicon on an SOI platform in the mid-IR range, free-standing silicon device structures fabricated by under-etching the BOX are reported [39, 40]. Various functional mid-IR devices based on silicon have been demonstrated, including waveguides, resonators, grating couplers, multi-mode interferometers (MMIs) and Mach−Zehnder interferometers (MZIs), arrayed waveguide gratings (AWGs), modulators, frequency combs and light sources, etc. For passive components, suspended waveguides with low-dispersion (±100 ps/nm/km) over a wavelength range of 2∼8 μm has been first demonstrated in 2012 [39] with a minimum waveguide loss of 3.0 ± 0.7 dB/cm, and a suspended ring resonator with Q factors of ∼10,000 and ∼8100 for near-IR and mid-IR were also reported. A subwavelength grating (SWG) coupler with a 24.7% coupling efficiency at 2.75 μm [40] and a 1 × 2 MMI-based wavelength demultiplexer with a low insertion loss of 1.2 dB at 2 μm [41] were demonstrated. For active components, a mid-IR TO modulator has been reported [42] using a spiral-based asymmetric MZI with aluminum heaters. The modulator operates at 3.8 μm with a 30.5-dB-high modulation depth, a 3-dB bandwidth of 23.8 kHz and a switching power of ∼47 mW. The first free-carrier injection-based mid-IR electro-optic (EO) modulator in SOI at 2.165 μm with a modulation speed up to 3 Gbit/s was demonstrated in 2012 [43]. The modulator has a $V_\pi \cdot L$ of 0.12 V mm with an extinction ratio of 23 dB. For nonlinear devices, a SOI ring-resonator−based on-chip frequency comb has been shown, with a spectrum spanning from 2.1 to 3.5 μm and a frequency spacing of about 127 GHz [44]. The ring resonator was fabricated using an etchless process, showing a loaded Q∼220,000 and an intrinsic Q∼590,000, respectively. In 2015, an octave-spanning mid-IR (1.5–3.3 μm) frequency comb was generated in a silicon nanophotonic wire waveguide on a room-temperature-operating CMOS-compatible chip [45]. In 2022, a single-mode mid-IR laser at 3.4 μm with a wide tuning range of 54 nm using a tunable high-Q silicon microring cavity and a multi-mode interband cascade laser(ICL) [46] was reported. The single-frequency lasing power reaches 0.4 mW via self-injection locking, with upper-bound effective linewidth estimated to be 9.1 MHz and a side mode suppression ratio of 25 dB. This chip-scale and tunable single mode high power mid-IR light source may be expanded to longer wavelength quantum-cascade lasers and lead to the development of compact, high-performance mid-IR sensors for spectroscopic applications. Because of the reduced nonlinear absorption, other nonlinear photonic functions such as parametric amplification [47] and wavelength conversion [48] have also been demonstrated in the short-wave IR and mid-IR. By engineering the waveguide cross-section and optical mode interaction with the absorptive cladding oxide to reduce loss at mid-IR wavelengths, a microring resonator with an ultrahigh Q factor of 10^6 at wavelengths from 3.5 to 3.8 μm has been reported, which was used for optical parametric oscillation with a low threshold of 5.2 mW [37]. These works pave the way for a wide working band from near-IR to mid-IR for silicon photonic devices.

2.1.2 Silicon nitride

Silicon nitride (Si_3N_4) is emerging as a promising material to complement silicon at wavelengths below 1.1 μm due to its wide optical bandgap and ultralow absorption loss. By changing the N/Si ratio, silicon nitride has an optical bandgap that can vary from 2.7 to 5.0 eV, covering a wide

transparency range from visible to mid-IR (∼300 nm−8 μm). It also has a moderately high nonlinear refractive index ($n_2 = 2.4 \times 10^{-19}$ m^2/W) which is ten times higher than silica, and most importantly semiconductor mass manufacturing compatibility [15, 19, 49]. By leveraging mature silicon fabrication techniques, it shows great promise for delivering low-cost, high-yield, small form-factor, and low-power consumption integrated photonic components. Some typical devices of Si_3N_4 are shown in Figure 2(b). Some typical devices of Si_3N_4 are shown in Figure 2(b) including a fabricated silicon nitride waveguide with smooth surfaces [50], a silicon nitride microring resonator coupled to a bus waveguide as an optical parametric oscillator [51] and a nanophotonic switch operating in the visible spectral range for sub-millisecond deep-brain optical stimulation [52]. There are two most common methods to deposit Si_3N_4 films, namely low-pressure chemical vapor deposition (LPCVD) and plasma-enhanced chemical vapor deposition (PECVD). These chemical vapor deposition processes depend on both chemical reactions and gas flow dynamics. In the LPCVD process, the important variables are pressure, temperature, flow rate, and gas ratio. In the PECVD process, in addition to these variables, RF power can also be varied. LPCVD Si_3N_4 films are deposited at high temperatures around 800 °C, and PECVD films are deposited at much lower temperatures around 300 °C−400 °C. While lower temperature has the benefit of enabling safe deposition on temperature-sensitive materials and devices, it has the disadvantages of producing films with higher optical loss due to higher N−H bonds absorption as well as lower density and higher roughness. Recently, reactive sputtering with DC-pulsed source using a silicon target under Ar/N_2 plasma environment at temperatures below 100 °C was developed which provides another promising way to deposited Si_3N_4 film at low temperature [53]. Similar to silicon, numerous structures such as waveguides, ring resonators, photonic crystals, grating couplers, inverse tapers, Y-junction splitters, and multimode interferometers have been demonstrated using Si_3N_4. The usage of Si_3N_4 as a slab waveguide can date back to 1970s [54, 55]. With advances in technology, various optimization methods to reduce the losses of Si_3N_4 waveguides have been developed, such as high-temperature thermal annealing, chemical mechanical polishing, improved plasma etching, multipass lithography, photonic damascene process, and so on. Taking the waveguide loss values around 1.55 μm to better illustrate the development, in 2005, a low loss down to 0.1 dB/cm was reported by using a waveguide with a height of 150 nm and a width of 800 nm [56]. In 2014, a loss less than 0.01 dB/cm was reported using a highly delocalized resonator with a height of 40 nm, a width of 11 μm and a bending radius of 9.65 mm [57]. In 2016, a low propagation loss of ∼0.021 dB/cm was achieved in a "finger-shaped" Si_3N_4 resonator with an intrinsic Q around 17 million [58]. In 2017, an ultralow loss (<0.01 dB/cm) was achieved using a high confinement resonator with a height of 730 nm, a width of 2.5 μm and a bending radius of 115 μm [50]. Similarly, the photonic Damascene process has been used to fabricate very thick silicon nitride films (0.8–1.75 μm) hosting waveguides with a loss <0.05 dB/m, sometimes combined with a reflow process [59, 60]. Nowadays, Si_3N_4 has been used in numerous fields including integrated frequency comb generation, communications, spectroscopy, light detection and ranging, optogenetics, biosensing, optical coherence tomography, photonics quantum circuits, on-chip delay lines, atomic clocks, optical phased arrays, and narrow linewidth lasers [52, 61–86].

2.1.3 Silica

Silica material has a bandgap of 9.3 eV, covering a wide transparency range from visible to mid-IR (∼200 nm−3.5 μm). Silica-on-silicon optical waveguides are one of the most popular choices for photonic integrated circuits due to the mature fabrication process, low cost, low propagation loss, and refractive index contrast matching with optical fibers [18]. A large number of silica waveguide devices have been used in commercial optical equipment owing to their excellent optical performance, such as 1 × N optical splitters and AWGs. Due to the low index contrast between the silica core layer and the cladding layer, extremely low propagation loss of 0.08 dB/m in the silica waveguide was demonstrated [87] and a chemically etched ultrahigh-Q wedge-resonator on a silicon chip [88] is shown in Figure 2(c). However, due to the low refractive index of silica (∼1.44), the bending radius typically needs to be tens of millimeters, which leads to large footprints of the silica waveguide devices that are not suitable for large-scale, high-density, and compact photonic integrated circuits [89].

2.2 Non-group IV materials on silicon

Emerging applications will drive the demand for photonic integration platforms, which support not only the near-IR window, but also the visible and mid-IR operation, and drive the silicon photonic integration from low power and passive oriented components toward the next generation of active, high-power handling, and high-nonlinearity components. Looking for new materials with wider transparency

windows, stronger electro-optic and nonlinear properties, and capability of supporting high-bandwidth modulation is inexorable for ultrahigh speed, energy-efficient communications and beyond. Additionally, materials that can be easily integrated with silicon photonics are attractive in terms of scalability and wide adoption. Some promising non-group IV materials and waveguides on silicon are the metal oxides (Al_2O_3, Ta_2O_3), direct bandgap materials (AIN and GaN), ferroelectric oxides (LN, BTO and PZT), and 2D materials. Table 2 summarizes the optical properties of the typical wideband materials which can be heterogeneously integrated on silicon.

2.2.1 Metal oxide (aluminum oxide (Al_2O_3, or alumina) and tantalum pentoxide (Ta_2O_5, or tantala))

When the operating wavelength in the visible band or below is desired, metal oxides including aluminum oxide (Al_2O_3, or alumina) and tantalum pentoxide (Ta_2O_5, or tantala) are widely explored. Al_2O_3 has a wide bandgap from 5.1 to 7.6 eV [90]. Thanks to atomic layer deposition (ALD) and sputter deposition [97], Al_2O_3 waveguides show great potential for low loss integration from the ultraviolet (UV) to visible (208 nm–633 nm) [98]. Figure 3(a) shows the representative devices of alumina on silicon platform with straight, bent waveguides, and fully-etched vertical grating couplers, in which a waveguide loss of <3 dB/cm at a wavelength of 371 nm and a ring resonator with an intrinsic quality factor (Q factor) $>4.7 \times 10^5$ at a wavelength of 405 nm have been demonstrated [90]. Ta_2O_5 has a theoretical bandgap of 4.4 eV with a transparency window close to 250 nm. The unique property of Ta_2O_5 is the low but sufficient refractive index contrast to an oxide cladding at UV wavelengths, so that the sidewall scattering losses can be suppressed due to the diluted optical modes, and the measured waveguide losses below 0.3 dB/cm at wavelengths close to 633 nm [91] (Figure 3(b)) and ∼0.03 dB/cm across the entire telecommunications C-band [99] have been demonstrated respectively. Now Ta_2O_5 is emerging as a strong competitor to Si_3N_4 waveguide in terms of high refractive index, large bandgap, low stress, low optical loss, low thermo-optic coefficient, and 3-fold higher nonlinearity. During the fabrication of oxide cladded Ta_2O_5 waveguides, Ta_2O_5 can be deposited to make thick cores (e.g. 800 nm–1 μm) without the stress cracking issues of stochiometric Si_3N_4. Due to crystallization of the material, the annealing temperature of Ta_2O_5 is limited to approximately 600 °C, far below ∼1200 °C of Si_3N_4 annealing temperature needed to drive out hydrogen to achieve ultralow loss. A lower waveguide loss at 1.55 μm in Ta_2O_5 waveguide (core thickness ∼90 nm) has been demonstrated compared to that of Si_3N_4 waveguide with an equivalent core thickness [99]. Ring resonator structure with an intrinsic Q value of 3.8 million at 633 nm has been reported [91]. Additionally, Ta_2O_5 has a higher optical nonlinear coefficient ($\chi^{(3)} = 2 \times 10^{-13}$ esu) [100], making it an attractive material for ultracompact and high optical confinement structures with wideband nonlinear applications

Table 2: Optical properties of typical wideband materials heterogeneously integrated on silicon platform.

Parameter	Al_2O_3	Ta_2O_5	AIN	GaN	LN	$BaTiO_3$	PZT
Experimental bandgap (eV)	5.1–7.6 [90]	4.4	6.0 (0.21 μm)	3.4	3.7 (0.34 μm)	3.2–3.3	3.35–3.89
Mean refractive Index(n) [$\lambda =$ 632 nm]	1.77	2.13	2.16	2.38	2.29	2.41	2.40
To coefficient (K^{-1})	2.75×10^{-5}	8.8×10^{-6} [91]	2.32×10^{-5}	5.0×10^{-5} [92, 93]	3.34×10^{-5}		
Kerr coefficient ($m^2\ W^{-1}$)		$6.2 \pm 2.3 \times 10^{-19}$ [91]	2.3×10^{-19}	3.4×10^{-18} [94, 95]	1.8×10^{-19}		8.5×10^{-18}
Pockels effect (pm/V)			0.67 (r_{13}) −0.59 (r_{33})	1.91 ± 0.35 (r_{33}) 0.57 ± 0.11 (r_{31})	31.8 (r_{33})	1640 (r_{42})	−157.1 (r_{33})
Typical waveguide loss (dB/cm) [$\lambda =$ 1.55 μm]	3 [$\lambda =$ 371 nm]	4.8–5.4	0.8			10.5 ± 0.2 (TE), 9.0 ± 0.4 (TM) [96]	1

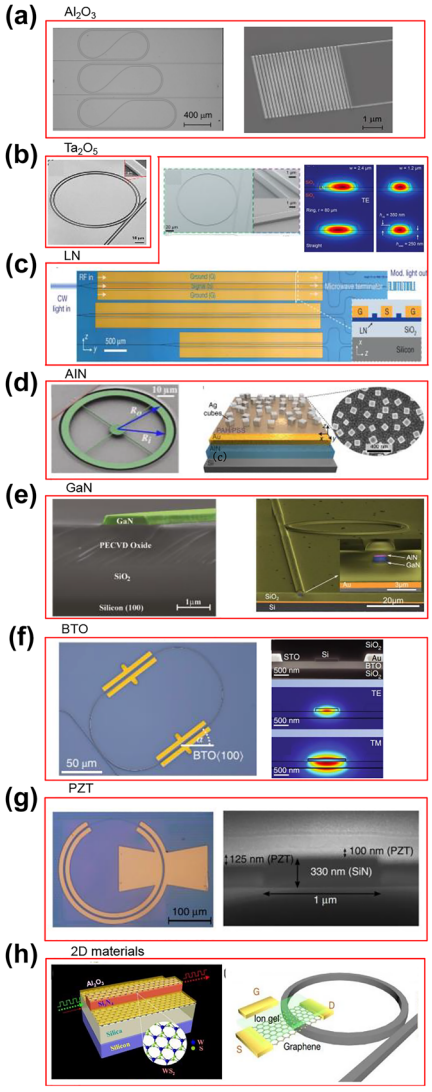

Figure 3: Representative devices of non-group-IV materials on silicon platform. (a) AI_2O_3: the SEMs of alumina straight, bent waveguides and fully-etched grating couplers [90]. (b) Ta_2O_5: a tantala resonator [91]. (c) LN: an ultrahigh Q LN microring resonator [109]; a CMOS compatible nanophotonic LN high speed modulator [112]. (d) AIN: an AlN suspended optomechanical microring resonator [126]; an AIN metasurface-pyroelectric detector [131]. (e) GaN: a cross-session SEM of GaN waveguide [141]; a GaN-on-insulator ring resonator on silicon [151]. (f) BTO: a BTO ring resonator with its cross-session SEM and TE/TM mode profiles [96]. (g) PZT: a PZT-on-SiN ring modulator [161]. (h) 2D materials: a schematic of the WS_2-based optical modulator structure [178]; a conceptual design of the gate-tunable graphene–nitride heterogeneous microcavity Kerr frequency combs [165]. [(a) Reproduced with permission from reference [90]. Copyright © 2020, society of photo-optical instrumentation engineers; (b) reproduced with permission from reference [91]. Copyright © 2021, optical society of America; (c) reproduced with permission from reference [109]. Copyright © 2017, optical society of America; reproduced with permission from reference [112]. Copyright © 2018, nature publishing group; (d) AIN: reproduced with permission from reference [126]. Copyright ©2012 American institute of physics. Reproduced with permission from reference [131].

including optical frequency combs and supercontinuum generation. Four-wave mixing experiments with high-confinement Ta_2O_5 waveguides and a relatively low optical loss of 1.5 dB/cm have been reported [101]. Al_2O_3 and Ta_2O_5 have also been actively studied in emerging applications, such as nanophotonic waveguide enhanced Raman spectroscopy (NWERS), in which the high index contrast waveguide excitation with visible light is critical [102]. The NWERS is a sensing technique involving the generation and detection of low levels of light, in which the level of background Raman autofluorescence from molecules in close vicinity of the waveguide is low compared to the desired Raman signal. Ahluwalia et al. [103] have compared both the Ta_2O_5 and Si_3N_4 waveguide Raman autofluorescence background with respect to their own background with excitation in the range 488–640 nm in direct stochastic optical reconstruction microscopy (dSTORM) for single molecule localization. At 640 nm, a comparable excitation background was observed between the two materials. However, at shorter wavelengths, Ta_2O_5 is expected to perform better as the background for Si_3N_4 significantly increases, which reduces the localization precision for dSTORM imaging.

2.2.2 Lithium niobate

Lithium niobate ($LiNbO_3$ or LN) has a wide transparency window from UV to mid-IR and low absorption loss. It has been the most successful optical material for commercial modulators due to its large nonlinear and electro-optic coefficients (non-centrosymmetric crystal with strong Pockels effect). LN modulators have been commercially available for decades along with the great success of optical fiber communications that underpin the internet [104]. The recent revolution in the LN photonic industry has been sparked by the thin-film lithium niobate (TFLN) waveguide with performance far exceeding the traditional bulk lithium niobate devices [104], especially with the innovations of nano-fabrication of LN-on-insulator (LNOI). With all these

good optical performances in the telecommunication band, LNOI opens an avenue to outperform bulky LN devices in footprint and cost, and realize integrated on-chip photonic devices with unprecedented performances in terms of propagation loss, optical nonlinearity, and electro-optic tunability. A typical LNOI wafer (3 or 4 inches) generally has a sub-micrometer LN film thickness (∼300–900 nm) and is suitable for mass production of nanostructure building blocks with ridge waveguide fabrication techniques. For the rib waveguides etched into the LN thin film layer and bonded on the buried silicon dioxide layer, the index contrast can vary between 0.7 and 1 with or without silica superstrate [105], offering benefits of compact mode size with low bending loss and small radius, high efficiency for electro-optic interaction, and nonlinear optical process with strong modal confinement [53, 106]. The TFLN based ridge waveguide by dry etching has shown a low loss of 0.3 dB/cm at 1.55 μm [107]. Furthermore, for waveguides fabricated by direct etching and by using CMP together, the surface roughness of LNOI nanostructures is around 0.1 nm [108]. A LN microring resonator with a record low loss of 0.027 dB/cm and ultrahigh Q factor of 10^7 [109] (Figure 3(c): left) and a resonator with a high Q of 11 million [110] have been demonstrated. A LNOI based modulator can also achieve high bandwidth, low drive voltage, low insertion loss, and compact size. Especially, compared with the value of 10–20 V cm of typical bulk LN modulators, a half-wave voltage-length product $V_\pi L$ of 2–3 V cm [111] has been demonstrated. A typical nanophotonic LN modulator compatible with CMOS drive voltage of $V_\pi = 1.4$ V and 3-dB electro-optic bandwidth up 100 GHz [112] is shown in Figure 3(c): right. Although lithium niobate has a wide transparency window ranging from UV to mid-IR and great progress has been made along the development of high-performance devices at telecom wavelengths in near-IR band, less work has been demonstrated for other wavelength ranges [106, 113]. Recently, an ultralow-loss integrated visible photonics platform based on thin-film LNOI has been demonstrated [110]. These demonstrated waveguides feature an ultralow propagation loss of 6 dB/m and the microring resonators feature a high intrinsic Q of 11 million at 637 nm wavelength. An on-chip visible light intensity modulator with an electro-optic bandwidth of 10 GHz was also demonstrated. The visible or mid-IR light in LNOI can also be generated by using wavelength up-conversion or down-conversion in telecom wavelengths as it possesses both large $\chi^{(2)}$ and $\chi^{(3)}$ nonlinearities and a wide transparency window from 0.3 to 5 μm. For example, the broadest supercontinuum generation (SCG) in a monolithic dispersion-engineered LN waveguide, spanning from 0.35 to 4.1 μm at a pulse energy of 240 pJ has been demonstrated [114]. The visible spectrum from 0.45 to 0.8 μm through second harmonic generation (SHG) and sum frequency generation (SFG), the UV spectra at 360 nm through cascaded SHG via phase-matching to higher spatial mode, and mid-IR combs from 3 to 4 μm via difference frequency generation (DFG) were observed. The near-UV light may be further generated based on Mg-doped LN. Ultralow-loss LN waveguides with strong second-order and third-order nonlinearities, together with the integration of on-chip light sources, may open up opportunities for various novel devices for frequency metrology, sensing and quantum information processing in UV, visible, and mid-IR regimes.

2.2.3 Aluminum nitride

Aluminum nitride (AlN) is another type of wideband semiconductor material that can be integrated on silicon platform. AlN has a large bandgap of 6.2 eV, a wide transparency window covering from UV to mid-IR, and a significant second-order nonlinear optical property contributed by its non-centrosymmetric crystal structure. AlN is a ceramic with low dielectric constant and excellent mechanical properties. It is non-toxic and has a linear expansion coefficient similar to that of silicon. In addition, it has high thermal conductivity and excellent electrical insulation properties, making it an ideal material for many electronic applications. Furthermore, it also exhibits piezoelectric and pyroelectric effects, which enable optomechanical devices and pyroelectric photodetectors. AlN on silicon has been widely used for sensors, actuators [115, 116], and also successfully demonstrated for UV LEDs [5]. Various standard functional devices such as couplers, waveguides, ring resonators, optomechanical devices, emitters, photodetectors, and metasurfaces have been demonstrated. In 2012, AlN-on-insulator has been proposed as a new material system for integrated optics by Pernice et al. [117]. AlN thin films were sputtered onto a 2.6 μm thick SiO_2 on silicon substrate. The AlN film is highly c-axis oriented with a rocking curve full-width at half-maximum of 2° at AlN's [0002] peak. The film thickness is chosen to be 330 nm on this platform and fabricated device propagation loss down to 0.8 dB/cm is reported at 1.55 μm. In 2014, the working wavelength of an AlN waveguide has been extended to the mid-IR wavelength regime ($\lambda = 2.5$ μm) with a propagation loss of 0.83 dB/cm [118]. In 2019, by leveraging the same sputtered AlN on SiO_2 platform, the working wavelength of the photonics devices has been further extended beyond 3 μm [119]. The electro-optic coefficient of AlN has been reported to be $r_{13} = 0.67$ pm/V, $r_{33} = -0.59$ pm/V (measured at 633 nm) [120], which despite

being significantly less than LN, could still be beneficial due to its ease of film deposition. Such an electro-optic effect enables the demonstration of phase shifters and optical modulators using AlN [121, 122].

Compared with thermo-optic-effect-based phase shifters, the electro-optic effect has the advantage of low power consumption and fast tuning speed. The electrodes are placed at the top and the bottom of the AlN waveguide. The maximum electric field created by the voltages applied on electrodes can go through the AlN waveguide. The modulation efficiency ($V_\pi \cdot L_\pi$ product) measured from the fabricated waveguide-ring resonators and MZI modulators near the 1.55 μm wavelength is ∼240 V cm for the transverse electric (TE) mode and ∼320 V cm for the transverse magnetic (TM) mode. Currently, the modulation speed is estimated to be 30 MHz which is limited by the speed of the voltage supplier. Besides, the modulation efficiency of the present AlN phase shifter is low due to the relatively small Pockels coefficient of AlN. The piezoelectric coefficient of AlN thin film has been reported to be $d_{33} = 5.53$ pm/V, $d_{31} = -2.65$ pm/V [123, 124]. Such piezoelectric property enables the wide utilization of AlN in MEMS [115, 116]. The piezoelectric property together with optical properties of AlN discussed earlier, make AlN a suitable material for optomechanical devices. A number of MEMS-based optomechanical devices have been demonstrated [125, 126]. Also, contributed by the piezoelectric property and photo-elastic constant ($p_{13} = -0.019, p_{33} = -0.107$ [127]), AlN has become a platform to investigate the photon–phonon interaction within solids [128]. Figure 3(d): left shows an optical micrograph of a suspended AlN ring resonator made adjacent to a straight coupling waveguide. A loaded Q of 125,000 is measured and three mechanical modes are found at 30.6 MHz, 47.3 MHz, and 1.04 GHz for this fabricated optomechanical device. The GHz AlN optomechanical resonators demonstrated in Ref. [119] can find applications in precision oscillators and high-speed ultrasensitive systems, as well as in acoustic nonreciprocal devices such as isolators. The pyroelectric coefficient of AlN has been reported to be 0.0033 μC/(cm^2 K) [129]. Such pyroelectric effect enables the realization of pyroelectric photodetector using AlN [130–132]. By integrating a plasmonic metasurface with an aluminium nitride pyroelectric thin film on Si substrate (schematic shown in Figure 3(d): right), spectrally selective, room-temperature pyroelectric detectors from 0.66 to 2 μm with an instrument-limited 1.7 ns full width at half maximum and 700 ps rise time are demonstrated. Heat generated from light absorption diffuses through the subwavelength absorber into the pyroelectric film producing responsivities up to 0.18 V W^{-1} due to the temperature-dependent spontaneous polarization of the pyroelectric films.

A significant second order nonlinear effect for AlN thin film has been reported on either sapphire or Si substrate. However, the second harmonic generation efficiency and $\chi^{(2)}$-based optical parametric generation are severely limited by the intrinsic propagation losses. Single-crystalline AlN epitaxially grown on sapphire substrate has demonstrated much lower loss compared with the polycrystalline AlN-based cavity [133, 134]. As a result, most of the nonlinear studies are conducted with the epitaxially growth single-crystalline high-quality AlN on sapphire substrate rather than using sputtering AlN on Si substrate, and it will not be discussed in detail here.

2.2.4 Gallium nitride

III-N family compounds such as GaN and its alloys – AlGaN and InGaN, are other promising candidates for integration on the silicon platform. They are favorable for light emitting devices (LEDs, LDs) [135, 136] due to their direct bandgap property, and their emission spans a wide range – from the UV to the visible and a wide transparency range from the UV to mid-IR [137]. GaN exhibits high breakdown voltage (>3 MV/cm) [138], moderate thermo-optic coefficient ($\sim 5 \times 10^{-5}$) [92, 93] and resilience to harsh environments – including elevated temperature, corrosive environment and ionizing radiation [139]. The ability to grow multilayer structures consisting of AlGaN and InGaN alloys enables high flexibility in band structure design as well as in finely tailoring the grown structure's refractive indices. Due to its wurzite non-centrosymetric structure, GaN also possesses 2nd order nonlinearity. Its $\chi^{(2)}$ coefficient was measured in bulk platform and in a waveguide configuration and values of around 10 pm/V were reported [140, 141]. Its third-order nonlinear coefficient is about an order of magnitude higher than that of Si_3N_4, LN, and AlN ($n_2 = 3.4 \times 10^{-18}$ m^2/W [94, 95]), leading to exciting opportunities in nonlinear photonics applications. GaN is epitaxially grown mostly using MOCVD, but there are some niche applications requiring MBE growth. The control of its high-quality epitaxial growth, doping and fabrication processes are in wide usage and are gaining maturity. The Nobel prize in physics in 2015 was awarded on the development of the GaN based blue LED [142]. It has led to a well-established industry and is the second most processed semiconductor after Si. Therefore, photonics based on GaN is appealing not only because of its unique characteristics, but also due to its solid industrial potential.

In order to integrate GaN on a Si substrate, direct growth is possible in principle with the aid of strain relief buffer layers [143, 144]. However, due to the lower RI in GaN than Si – 2.3 compared to 3.7 at 1.55 μm, a few micron of SiO_2 is necessary between the layers as an optical isolating layer. Therefore, wafer bonding approach is preferred, resulting in a GaN on insulator (GaNOI) on silicon platform.

Many passive photonic devices have been demonstrated on GaN platform, including low loss waveguides [95, 145], directional couplers [146], frequency converters [141, 147] and more [148]. Waveguides and resonators with propagation losses as low as 1 dB/cm [145] and 0.26 dB/cm [149] (respectively) were reported at telecom wavelengths. In the visible range, loss values of ∼2 dB/cm were reported [150]. On-chip nonlinear optical devices were demonstrated, utilizing the wide bandgap of GaN and the fact that TPA is negligible for wavelengths above 730 nm. The typical GaN devices of waveguide and resonator are shown in Figure 3(e), and second harmonic generation from 1.56 μm to 780 nm has been demonstrated by Xiong et al. [141] and by Gromovyi et al. [151] on GaNOI platform, respectively. GaN electro-optic coefficient (Pockels) has been reported to be $r_{13} = 0.5$ pm/V, $r_{33} = 1.9$ pm/V [152]. Few theoretical works were done in the design of active devices such as modulators and phase shifters [153, 154]. However, unlike AlN, such devices have not been experimentally demonstrated yet.

2.2.5 BTO

Barium titanate (BTO) has a bandgap of 3.2–3.3 eV. It has garnered substantial interest in the past few years due to the very high $\chi^{(2)}$, which leads to a large bulk Pockels coefficient >1600 pm/V, approximately 50 times higher than LN. However, previous attempts to integrate them with MgO waveguides degraded their effective $\chi^{(2)}$ by one or more orders of magnitude [155], or were limited to slow speeds <1 MHz [156]. This is partially because that the $\chi^{(2)}$ depends on the non-centrosymmetric crystalline structure of the material, and this effective non-centrosymmetry can be reduced by random orientations of domains formed during growth by pulsed layer deposition, molecular beam epitaxy (MBE) or metal-organic CVD (MOCVD). While photonic crystal structures have achieved higher modulation bandwidths of 4.5 GHz using 500-nm thick MOCVD films of BTO, they were restricted to MgO substrates [157]. Recent work has used MBE-grown BTO films wafer bonded to silicon to overcome these challenges, leading to large Pockels coefficients >900 pm/V [96]. The BTO ring resonator with its cross-sessional SEM and TE/TM mode profiles are shown in Figure 3(f). The films had a substantial fraction of the optical field (∼40%) in just 50 nm thin BTO films despite its lower index than silicon. All these improvements led to a high analog modulation bandwidth of 30 GHz. The current state-of-the-art loss is about 6–10 dB/cm [158]. Even though the absorption edge of BTO is reported around 300 nm, due to the high losses, the number of reported works about BTO devices on silicon substrates are very limited. As progress in BTO-Si devices has demonstrated cryogenic operation [159] and non-volatile memory implementations [160], future developments would need to reduce the propagation losses significantly.

2.2.6 PZT

Piezoelectric lead zirconate titanate (PZT) has a bandgap ranging from 3.35 to 3.89 eV and it is another type of material with large Pockels effect. Its Pockels effect is several times higher than that of LN. PZT thin films also show propagation losses down to 1 dB/cm and have been successfully integrated with silicon nitride films to demonstrate Pockels modulators with a 33-GHz analog bandwidth [161], as shown in Figure 3(g). The lower loss is achievable both due to the PZT material itself as well as the lower absorption and scattering loss in the silicon nitride substrate. Previous works have shown phase modulation at sub-MHz speeds using PZT-on-silicon nitride films but with significantly lower sub-MHz bandwidths, although wafer scale foundry compatible fabrication has been demonstrated in some of these works. Another attractive feature of PZT films is the ease of direct deposition on nearly any substrate through spin-coating and annealing (also called sol–gel), which is compatible with CMOS front-of-the-line processes [161]. This is simpler than wafer bonding of crystalline or epitaxially grown films that is needed for other $\chi^{(2)}$ materials such as lithium niobate or barium titanate. Future improvements could look at further reducing the losses, increasing modulation bandwidths and effective Pockels coefficients (currently at ∼150–250 pm/V) [162] through optimized waveguide design, placement of electrodes, or modifications to the stoichiometry of the material by incorporating suitable lanthanides [163].

2.2.7 2D materials

Another main development of wideband silicon photonics is the integration of two-dimensional (2D) materials on the silicon platform. 2D materials, including graphene, black phosphorus (BP), and tungsten disulfide (WS_2), etc., are the 3D crystals in the form of a planar structure regarded

as with a negligible thickness in one dimension. 2D materials have shown fascinating optoelectronic properties in windows ranging from visible to mid-IR due to their rich band structures from 0 to several eV [164], and demonstrated attractive optical properties that enable the generation, manipulation, and detection of light [164]. Thanks to their unique atomic flexibility, various 2D materials are conveniently integrated on silicon-based platforms without significantly affecting the mode fields, either on-chip [165] or on-fiber [166]. Of which, graphene is a single atom thick carbon sheet with atoms arranged in a hexagonal structure, and was first and most widely studied for integrated optoelectronic devices due to its excellent optical and electrical properties [167]. A mono-graphene layer has a wide transparency wavelength ranging from infrared to visible due to a constant absorption of 2.3%. It also has a high thermal conductivity (5300 W m^{-1} K^{-1}) and a high carrier mobility of 2×10^5 cm^2 V^{-1} s^{-1} at room temperature with electrical-controllable permittivity. Additionally, graphene has a large Kerr coefficient ($n_2 = 10^{-12}$ m^2 W^{-2}) which is highly favorable in nonlinear photonics [164]. The combination of 2D materials and silicon photonics has been bringing unprecedented new opportunities for silicon-based photonic devices, from lasers, modulators, photodetectors to nonlinear devices. 2D material based lasers on silicon platforms have been realized and mainly include two categories, one is the saturable absorption effect of 2D materials to achieve Q switched or mode-locked pulse output [168], and the other one uses 2D materials as gain media for actuation [169]. As saturable absorbers (SAs), 2D materials have achieved mode-locking of different lasers, covering different wavelengths from visible to mid-IR (500 nm–2.5 μm) [170]. For instance, Bharathan et al. report on the feasibility of MXene and platinum diselenide ($PtSe_2$) as novel saturable absorbers for the development of wavelength stabilized passively mode-locked mid-infrared fiber laser systems [171]. Besides, laser excitation based on WSe_2 [172], WS_2 [173], $MoTe_2$ [174] and MoS_2/WSe_2 heterostructure [175] have also been achieved within various silicon-based microcavities. 2D material based silicon modulators demonstrate ultrafast and broadband responses [176]. For instance, by integrating graphene heterostructures in silicon nitride microrings, Phare et al. achieved an electrically tuned resonance spectral shift, leading to ultrafast electro-optic modulation with a 30-GHz bandwidth [177]. More recently, Yang et al. integrated WS_2 with a silicon nitride waveguide and successfully achieved all-optical modulation and amplification of optical signals at 640 nm by modulating a 532 nm pump light source [178], as shown in Figure 3(h): left. Here, WS_2 can be used as a gain medium, which theoretically incurs lower loss and exhibits higher contrast level and signal-to-noise ratio. To date, versatile 2D materials-based modulators including different materials (e.g. graphene, TMDs, BPs, and other types) and different modulation mechanisms (e.g. optical, electrical, and thermal) cover the visible, infrared, and terahertz ranges [179, 180]. Photodetectors based on 2D materials was firstly reported by Xia et al. in 2009 [181]. Compared to traditional semiconductor photodetectors, 2D materials based photodetectors demonstrate appealing advantage in terms of bandwidth, possibly exceeding 500 GHz [182]. In 2D material photodetectors, the absorbed optical signals can be converted into electrical signals through a variety of physical mechanisms [183], such as the photothermalelectric effect (PTE), the photo-bolometric effect (PBE), the photoconductive effect (PCE) and the photovoltaic effect (PVE). In 2018, by interconnecting quasi-one-dimensional nanoribbons to form plasmonic resonator arrays, Guo et al. demonstrated a mid-infrared graphene detector, enabling the electrical detection of plasmon decay in the nearby graphene resonators with an external responsivity of 16 mA W^{-1} and a low noise-equivalent power of 1.3 nW $Hz^{-1/2}$ at 12.2 μm [184]. Later, Liang et al. reported a high-performance ultra-wideband photodetector based on PdSe2 with a unique pentagonal atomic structure, obtaining response from visible to mid-infrared range (up to ≈4.05 μm). The device stably operates in ambient and at room temperature, with a responsivity of 708 A/W at the wavelength of 1.064 μm [185] due to the photogating effect in 2D materials. Recently, Wu et al. designed a vertically stacked back-to-back 2D/3D hybrid photodetector using a black phosphorus (BPs)/molybdenum sulfide (MoS2)/silicon (Si) vdWs heterostructure in temporal-spatial coexisting near-IR/mid-IR two-color blackbody sensitive photodetectors, and showed ultralow crosstalk of ∼0.05% at room temperature [186]. 2D materials can also help to break the limitation that the nonlinear response in conventional integrated photonics is typically low. In 2018, using a graphene incorporated microring, Yao et al. reported controllably diverse gate-tunable graphene–nitride heterogeneous microcavity Kerr frequency combs in one single device [165], a conceptual design is shown in Figure 3(h): right. Furthermore, by integrating graphene in different optical paths (e.g. waveguides [187], integrated D-shaped fibres [188, 189] and silica microspheres [9]), researchers also accomplished the modulation of the second-order, third-order nonlinearity and group index of graphene, achieving tunable plasmonic generators and high performance sensors. Recently, via depositing a monolayer of crystalline Mo_3Te_4 in a 1-THz-FSR Si_3N_4 microcavity, He et al. demonstrated a 2D material enhanced

microcavity that can have a third order nonlinear susceptibility $\chi^{(3)} = 10^{-18} \sim 10^{-15}$ esu, potentially useful to ultralow threshold frequency conversion applications [190]. It can be seen that the 2D materials will become more attractive over the next few years covering a wideband as the fabrication maturity and control of the material properties increase rapidly.

To conclude this part, the integration of wideband material on silicon platform can enable new functionalities and play a critical role in the integration of light source, detectors, and the operation of devices not only near-IR but covering the visible and mid-IR range. Figure 3 shows the typical optoelectronic devices based on non-group-IV family materials on silicon platform. Yet, there are a relatively low number activities and reports on this platform, leaving room for further research with great potential applications.

2.3 General fabrication method and low loss process treatment

The general fabrication method and low loss process treatment of different optical materials on the silicon platform are illustrated in Figure 4(a). For these deposited thin film waveguide-based materials on insulator wafer (silicon, Si_3N_4, AlN, GaN, Al_2O_3, LN, $BaTiO_3$, and PZT), they generally follow the same fabrication process. First, a waveguide layer is deposited on to the silicon substrate; SiO_2 is the most commonly used insulating material on silicon due to its relatively low refractive index and ease to fabricate. Then the waveguide layer is patterned using lithography, such as e-beam lithography (EBL), deep-ultraviolet (DUV) lithography, and contact lithography. After exposure and the resist is developed, the design pattern is ready for transfer. Etch is used to transfer the pattern from the resist to the underlying waveguide layer. Depending on the materials and the ultimate goals, it can be dry etch or wet etch. Dry etch typically etches quickly and anisotropically, it is particularly useful for etching chemically resistant materials. After successfully transferring the patterns, the leftover resist is stripped, and cladding material is deposited to protect the waveguide layer. At this stage, the wafer is ready for dicing or further processing such as heater deposition, metal pad deposition, heterogenous integration, etc. Low-loss waveguide is the key to achieve high-performance integrated optoelectronic devices. Waveguide layer deposition, lithography and etch are the three key process steps to determine the loss. Many groups have been working on these steps to reduce the devices' losses. We have listed a few methods that can help to achieve low loss as shown in Figure 4(b). As an effective process, chemical mechanical polishing (CMP) is widely used to reduce thin film surface roughness, thus reducing scattering. In addition, during the LN fabrication

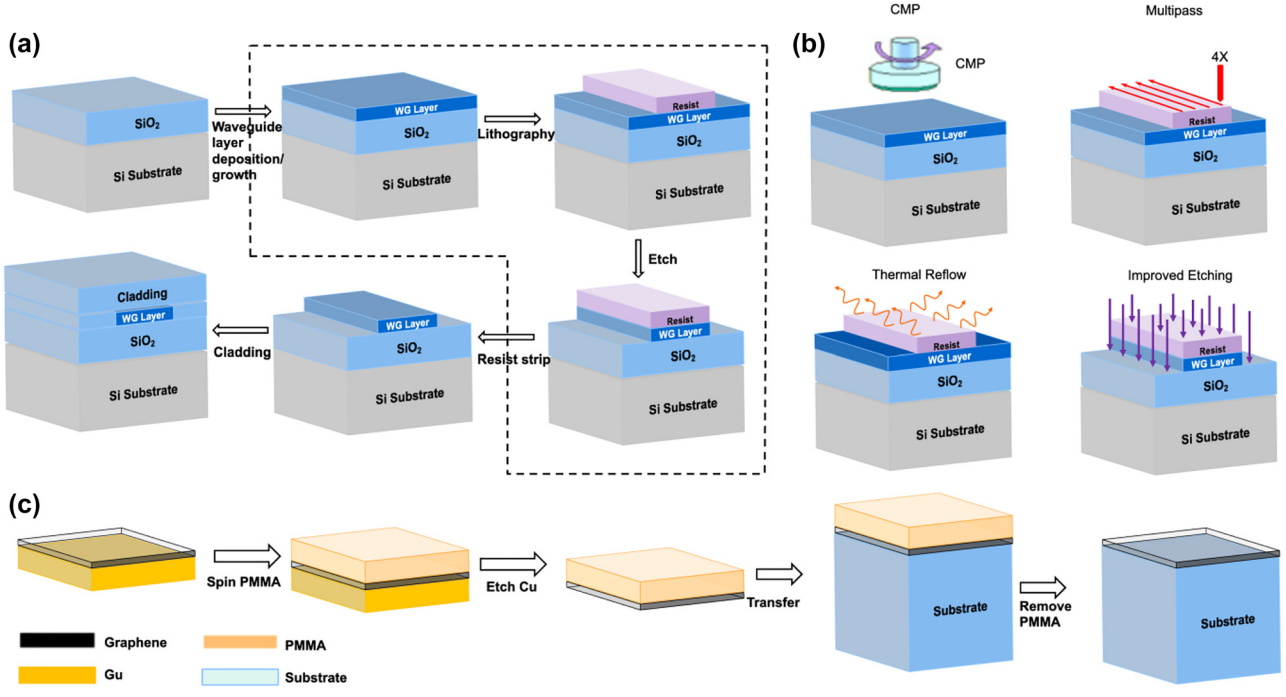

Figure 4: General fabrication method and low loss process treatment. (a) General fabrication method. (b) Low loss process treatment. (c) The fabrication process for 2D material integrated optoelectronic devices on a silicon platform based on the wet-transfer technique.

process, CMP has also been used to polish the sidewalls of the waveguide to reduce the scattering loss. In this process, a chromium layer is used as the CMP mask, and the pattern is formed by femtosecond laser ablation to define the shape of the LN waveguide. Then, by using a wafer polishing machine, the exposed LN film can be removed to form the waveguide. Finally, the chromium layer at the top of the LN waveguide can be removed by wet etch using HF solution. The sidewall angle of the LN waveguide can be adjusted from a few degrees to nearly 80° by controlling the duration of CMP process [191]. A second CMP process can be performed if the upper surface of the waveguide is very smooth, a root-mean-square surface roughness as low as 0.452 nm, and a low loss of 0.1 dB/cm has been demonstrated [108]. Other methods have been developed to reduce losses, such as multi-pass lithography to reduce line-edge roughness by exposing the same pattern multiple times, improved etch recipe to reduce polymer residue by optimizing the gas ratio, and resist reflow to provide smoother sidewalls by using tens of hours of high-temperature annealing.

The fabrication process for 2D material integrated optoelectronic devices on a silicon platform is a special process and it is commonly based on the wet-transfer technique, as shown in Figure 4(c). Taking graphene as an example, a polymethyl methacrylate (PMMA) layer is spin-coated on the graphene during the wet-transfer process, and the copper foil is etched by a commercially available etchant (copper etchant Type CE-100, or a 0.1 m $(NH_4)_2S_2O_8$, or ferric chloride ($FeCl_3$) solution). Then, the PMMA-graphene film is moved to distilled water to rinse the etchant residue. Subsequently, the film is transferred to the substrate, and the chip is dried overnight in air. Finally, the PMMA can be removed by acetone, and then the entire chip is covered with graphene layer.

Following the successful model of SOI foundry, ultra-wideband integrated photonics on silicon platforms are highly desired that are compatible with cost-effective wafer-scale fashion for more emerging applications. They are most likely to support heterogeneous integration of multiple wide bandgap material systems. However, the waveguide loss sets a fundamental limit to the performances of the integrated devices. The loss of a waveguide mainly includes the absorption loss, radiation loss and scattering loss. While the regime of ultralow loss has been achieved at telecom band, progress at wideband spectrum covering visible and mid-IR wavelengths is limited, because SOI platform is almost opaque or suffers from large absorption loss. To date, there are only a few materials that are highly transparent over the entire UV-to-visible spectrum. In the short wavelength range down to visible, the Rayleigh scattering from the waveguide roughness due to the non-idealities of fabrication will inevitably induce loss, which contributes significantly at the lower end of the visible band when scaling with the wavelength λ (as $1/\lambda^4$). Therefore, it is necessary to use materials that can be fabricated with low roughness to develop low-loss integrated photonic devices in the visible range. In the long wavelength range up to mid-IR, due to the strong absorption of the buried oxide in the range between 2.6 μm and 2.9 μm and beyond 3.6 μm, the development of low-loss waveguide is also immature. To enable the advances in visible and mid-IR

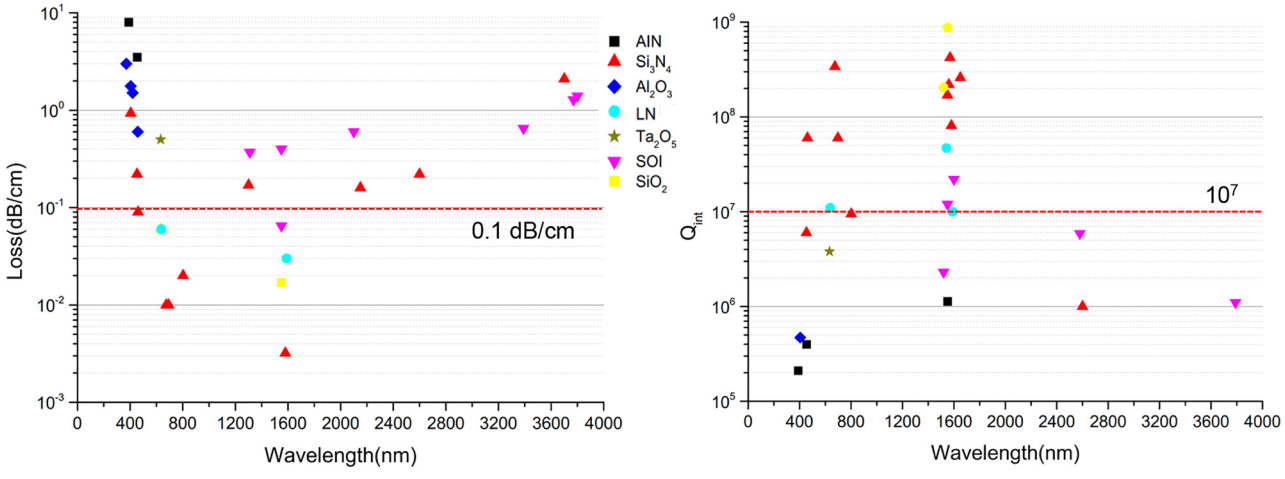

Figure 5: Summary of reprehensive waveguide losses and intrinsic Q factors of different optical materials on silicon platform across visible, near IR, and mid-IR spectra. (left) Waveguide loss of SiO_2 [192], silicon and SOI [39, 194–199, 202], Si_3N_4 [50, 57, 203–208, 210], AlN [210], Al_2O_3 [90, 204], Ta_2O_5 [91], and LN [109, 110]. (right) Intrinsic *Q* values in different optical materials of SiO_2 [88, 193], silicon and SOI [37,39, 200–202], Si_3N_4 [50, 57, 203, 205, 207, 209, 211], AlN [212, 213], Al_2O_3 [90, 214], Ta_2O_5 [91], and LN [109, 110, 215].

band, it is expected that the integrated solution should be CMOS compatible at wafer scale, capable of supporting various photonic components, with fundamental ultralow waveguide losses (<0.1 dB/cm), and ultrahigh Q resonators (>10^7). Here, in Figure 5 we summarize the representative low-loss and high intrinsic Q factor of aforementioned silicon based material or wide bandgap waveguide core material choices in the visible, near-IR and mid-IR range, including SiO_2 [88, 192, 193], silicon, and SOI [37, 39, 44, 194–202], Si_3N_4 [57, 203–211], AlN [212, 213], Al_2O_3 [90, 204, 214], Ta_2O_5 [91], and LN [109, 110, 215]. It can be seen that most of the impressive works still focus on the near-IR range. The waveguide loss and Q factors lag behind in the visible and mid-IR range. However, currently Si_3N_4 has been shown to be the most mature and versatile wide bandgap material covering visible and mid-IR bands with low propagation losses for the wavelengths ranging from 532 nm to 3.7 μm. Other non-group IV materials are still relatively undeveloped with fewer reports, but may excel in certain functions due to the unique properties aforementioned. Importantly, there are no one-fit-for-all solutions for high performance photonic devices from visible to mid-IR on silicon platform. The key factor to choose different wide bandgap materials for heterogenous integration include the optical properties (intrinsic material absorption in the core, cladding and substrate, nonlinearity and electro-optical properties, etc.) and the delicate waveguide design and fabrication process (optical confinement, waveguide side/top-wall scattering, etc.).

3 Typical visible, near-IR, and mid-IR applications

There is no doubt that telecommunication is the most successful application for silicon photonics. With the advantages of natural transparency in near-IR and CMOS compatibility, and spurred by the well-developed fiber as well as the erbium-doped fiber amplifier (EDFA) technologies, silicon photonics has started from its roots in telecommunication applications and has made remarkable development since its inception in the 1980s [216]. Numerous researches have been demonstrated in silicon photonics with various high-performance components in the telecommunication band [25, 35, 217, 218], i.e. waveguide, modulator, AWG, photodiodes, etc., and now reached sufficient maturity for commercial telecommunication applications at production volumes [26, 27, 35]. Now it has been extended to a plethora of application fields covering visible, near-IR, and mid-IR bands. However, silicon has well-known shortcomings in terms of limited wavelength range, lack of second-order optical nonlinearity, TPA and nonlinear absorption, etc. This promotes the integration of other aforementioned wideband materials on the silicon platform. Here we will focus on three typical wideband application scenarios as examples.

3.1 Integrated sensing and imaging technologies

Sensing is a field which greatly benefits from integrated optical components, especially photonic devices based on the silicon platform. These devices provide incomparable advantages such as high sensitivity, integration ability with electronic devices, compact footprint, low-cost, and semiconductor mass manufacturing compatibility. Waveguide-based devices and ring resonators are becoming more and more attractive in sensing applications such as chemical and biosensing. They are typically based on the variation of optical properties in the waveguide or ring resonator. When light propagates into an optical waveguide, a certain amount of power travels into the core, while the remainder is confined to the cladding and substrate regions which is called the evanescent field. In most cases, the evanescent field interacts with the analyte near the surface, and the effective index or absorption coefficient will be changed. As a result, various gases and chemical species can be detected. In other systems, the light is emitted or collected through photonic integrated circuits so that the phase and amplitude of the light and the delay introduced during its propagation can be measured. One example in bioimaging and health care is known as optical coherence tomography (OCT) which uses low-coherence light through fibers or photonic integrated circuits to capture the cross-sectional and three-dimensional images with micrometer resolution.

The visible spectral region is of particular interest for biosensing and imaging. However, silicon only offers good transmittance starting from 1.2 μm, and because of the relatively low refractive index of SiO_2, Si_3N_4 becomes more attractive. Highly accurate sensors based on Si_3N_4 have been reported for chemical and biological samples, such as DNA biosensor, methane sensor, and fluorescence-based sensors [219–222]. Other than these sensors, many efforts have also been made to address the need for simplification and miniaturization of sensing system parts using photonic integration, such as absorption and hyperspectral microscopes, cytometers, and OCT systems [62, 223–226]. Figure 6(a) shows the schematic of the bio-sensing using optical micro-resonators.

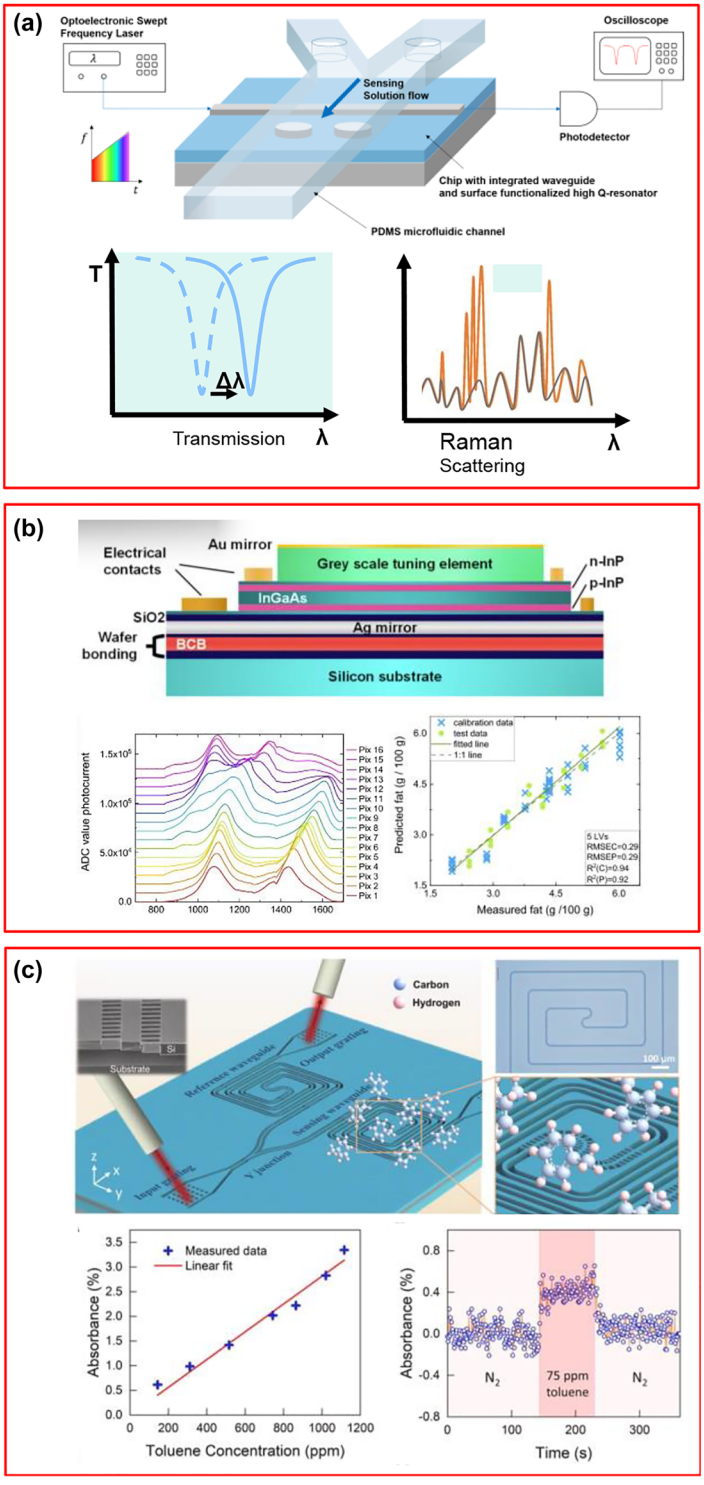

Figure 6: Typical integrated sensing devices. (a) Schematic of bio-sensing using optical micro-resonators [234]. (b) An array of resonant-cavity-enhanced photodetectors suitable for diffuse transmittance/reflectance measurements in the 850 nm–1.7 µm wavelength ranges on silicon substrate and the use of the multi-pixel array for the measurement of the nutritional properties of milk is presented [227]. (c) Example of mid-IR sensing based on the suspended silicon waveguide platform. Toluene vapor detection is presented with a corresponding limit of detection of 75 ppm. The response and recovery time to 75 ppm toluene are about 0.8 and 3.4 s, respectively [233]. [(a) Reproduced from website [234] http://www.its.caltech.edu/%7Eaphyariv/research.html; (b) reproduced with permission from reference [227]. Copyright © 2018, nature publishing group. (c) Reproduced with permission from reference [233]. Copyright © 2021, De Gruyter].

The near-IR spectral region is interesting for the sensing of organic materials due to the presence of absorption bands caused by overtones and combinations of vibrational modes of O–H, C–H, and N–H bonds. Near-IR can provide higher sensitivity than visible solutions for important application cases such as food science and health care. As an example, an array of resonant-cavity-enhanced photodetectors suitable for diffuse transmittance/reflectance measurements in the 850 nm–1.7 μm wavelength range is recently demonstrated on silicon substrate, as shown in Figure 6(b). The use of the multi-pixel array for the measurement of the nutritional properties of milk is presented [227]. In addition, near-IR is ideal for 3D imaging applications because it is invisible to the human eye, making it unnoticeable when cast into a user's face, eyes, or environment. Applications such as eye-tracking, short-range and long-range automotive Lidar, and non-invasive detection for point-of-care are all relied on the near-IR wavelength range.

The mid-IR spectral region is known as the molecular-fingerprint region. Most molecules have strong fundamental vibrational bands there, thus providing a unique way to identify and quantify molecules. The strength of transitions in this spectral band may be more than a thousand-fold stronger than that in the near-IR telecom region, enhancing detection sensitivity by a similar proportion. Silicon photonics has long been considered unsuitable for mid-IR applications due to its lack of broad transparency beyond the near-IR range. The transparency window of the silicon waveguide core extends to 6–8 μm wavelength, whereas the SiO_2 cladding material begins absorbing strongly around 3.5 μm. Therefore, few demonstrations of SOI waveguides have operated past 2.5 μm. To circumvent the limitation, efforts have been made to replace the lossy SiO_2 cladding with other materials exemplified by silicon-on-nitride or with air cladding suspended silicon structures. With these efforts, the wavelength limit has been pushed beyond 3.5 μm [37, 45, 228–232] and these structures can be used for gas sensing. For example, sensing based on the suspended silicon waveguide platform is demonstrated in Figure 6(c) [233]. Another example is CO_2 sensing. The absorption coefficient of the pure concentration CO_2 is larger than 80 cm^{-1} at the mid-IR wavelength around 4.3 μm. This strong absorption gives the ability to achieve the high sensitivity sensing of CO_2 with the mid-IR photonics. A CO_2 gas sensing structure based on a silicon-on-nitride strip waveguide was developed and the achieved limit of detection was 5000 ppm CO_2 at 4.23 μm [232].

3.2 Integrated optical frequency comb technologies

Optical frequency combs (OFCs) can offer an unrivalled degree of frequency measurement precision that underpins the advance of modern technology in both fundamental research and industry applications. By leveraging wide bandgap nonlinear optical materials, tightly-confined waveguide geometry and wafer-scale photonic foundries, the integrated OFC technology provides a novel route to realize compact, low-cost, and energy-efficient light sources with ultra-wideband properties ranging from visible to mid-IR, potentially revolutionizing the fields of information processing [7, 8], time–frequency metrology [3, 4], sensing [9] and quantum photonics [2].

OFCs are usually realized by optically pumping the optical media with strong nonlinearity, generating a phase-coherent light source with spectra of discrete, evenly spaced narrow optical laser lines [235]. The OFCs' bandwidths can be extremely broad thanks to the nonlinear optical interactions. These interactions can generate a broad range of new optical frequencies significantly beyond those in the initial laser field incident on the nonlinear medium. Starting from the traditional mode-locked laser (MLL) [236], OFCs have evolved into one of the most active areas in photonics. The most remarkable examples of generating such broad spectra light sources are supercontinuum generation (SCG) in optical waveguides, Kerr-comb generation (KCG) through Kerr nonlinear process $\chi^{(3)}$ in microresonators [51, 165, 169, 237–262], electro-Optical combs in modulators and quadratic combs through cascaded second harmonic generation $\chi^{(2)}$ process or $\chi^{(2)}$-based spectrum translation. Vast reviews in the OFCs can be found [263, 264]. Due to the abundant nonlinearity of wide bandgap semiconductors, both silicon-family related materials (from silica [265–267], Si_3N_4 [86, 245, 268], to silicon carbide (SiC) [269]), and non-group IV materials on silicon platform (i.e. 2D materials [165], Ta_2O_5 [91], AIN [270], LN,) have been utilized toward realizing chip-scale OFCs to generate hundreds of frequencies spanning tens of terahertz range from visible to mid-IR. Most of the aforementioned OFC demonstrations focus on the near-IR and mid-IR ranges, which are now relatively mature. However, visible OFCs are limited by strong material dispersion and high losses at short wavelengths. One way proposed to overcome these obstacles is to generate a parametric frequency comb in the near-IR and then convert it into visible region through second harmonic generation $\chi^{(2)}$ [270, 271]. Another approach is to use high-order mode to tailor the material dispersion [272]. Supercontinuum light generation has also shown promise for ultra-wideband frequency generation down to visible. The spectrum coverage

for representative works using different comb-generation approaches is shown in Figure 7(a).

Benefiting from the excellent characteristics of OFCs including high repetition rate, high coherence, and wide frequency spectrum, silicon-based soliton microcomb devices have unique advantages in communications, ranging, microwave generation [254, 258, 273], spectroscopy, and quantum applications [2]. Here, we show some examples. For optical communication, Geng et al. cloned and regenerated the soliton micro comb 50 km away through pump laser transmission and two-point locking, and used them as the local oscillators (LOs) of the receiver to retain the original frequency and phase characteristics, as shown in Figure 7(b). In the acquisition of coherent data demodulation, the steps of electrical frequency offset estimation and carrier phase estimation based on digital signal processing can be greatly simplified, and terabit coherent data interconnection can be realized [274]. For optical ranging and metrology, Jang et al. reported spectrally resolved laser dimensional metrology via a free-running soliton frequency microcomb with nanometric-scale precision, by employing a hybrid timing signal from comb-line homodyne, microcomb, and background amplified spontaneous emission spectrally resolved interferometry [247], as shown

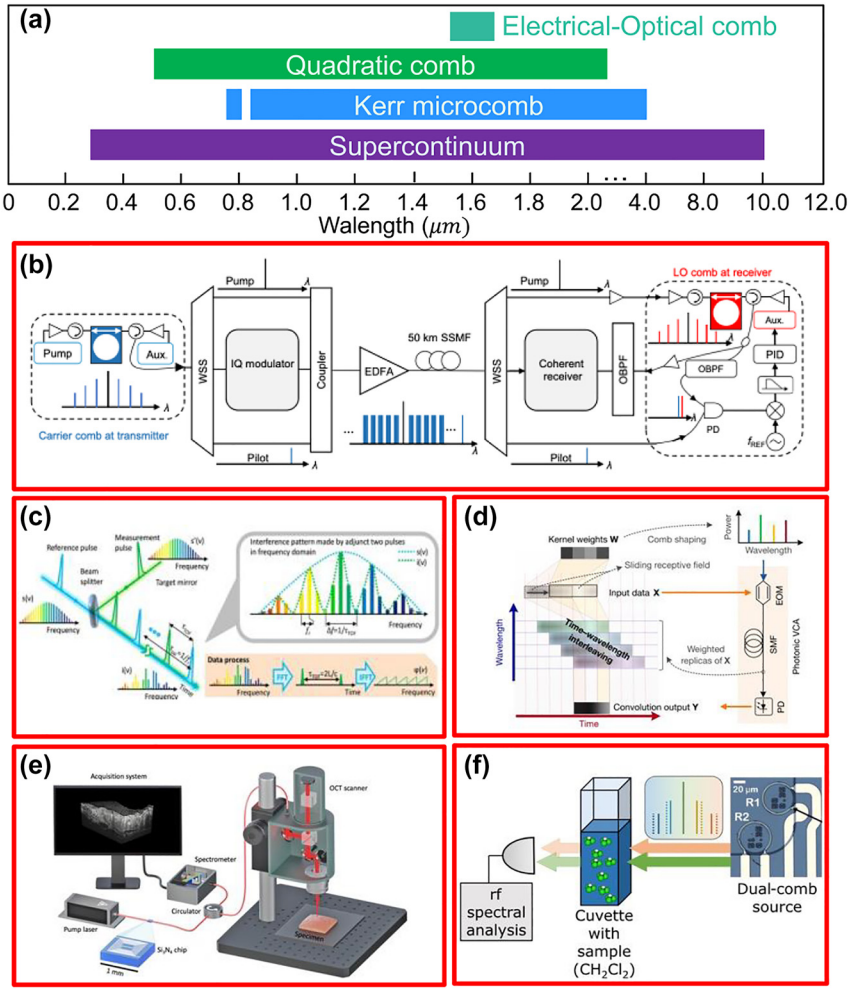

Figure 7: Typical OFC applications. (a) Map of the spectrum coverage for representative works using different comb-generation approaches (strips). (b) Optical interconnect using coherence-cloned DKS microcombs as carriers and Los [274]. (c) Architectural approach of the spectrally resolved ranging via soliton microcomb [247]. (d) Optical vector convolutional accelerator powered by a soliton crystal microcomb [7]. (e) Spectral domain OCT enabled by the generated SCG [225]. (f) Dual-comb spectroscopy using two microresonator combs generation [67]. [(b) Reproduced with permission from reference [274]. Copyright © 2022, nature publishing group. (c) Reproduced with permission from reference [247]. Copyright © 2021, American physical society. (d) Reproduced with permission from reference [7]. Copyright © 2021, nature publishing group. (e) Reproduced with permission from reference [225]. Copyright © 2021, AAAS. (f) Reproduced with permission from reference [67]. Copyright © 2018, AAAS].

in Figure 7(c). Li et al. unraveled the transitional dynamics of frequency microcombs from chaotic background routes to femtosecond mode-locking in real time [259]. For optical computing, Moss et al. demonstrated that the exciting photonic neural network processor using microcomb parallelization holds promise in surpassing the speed and energy efficiency of cutting-edge graphics processing units [7]. Powered by a soliton crystal microcomb (spacing of ~48.9 GHz) with 90 wavelengths occupying 36 nm across the C-band, the universal optical vector convolutional accelerator (see Figure 7(d)) operating at more than 11 Tera Operations Per Second (TOPS)has been achieved, demonstrating convolutions of images with 250,000 pixels for facial image recognition and 88 per cent accuracy for handwritten digit images recognition. For optical spectroscopy, Ji et al. [225] demonstrated a SCG platform based on a 1-mm^2 Si_3N_4 photonic chip for spectral domain OCT, as shown in Figure 7(e). The generated SCG has a flat 3-dB bandwidth of 105 nm near 1.3 μm without any postfiltering. The image breast tissue has been used to demonstrate strong imaging performance with 105-dB sensitivity and 1.81-mm 6-dB sensitivity roll-off with 300-μW optical power on sample. Dual-comb spectroscopy (DCS) uses heterodyne beating between two frequency combs with slightly different repetition rates to generate a sequence of beat notes, which down-converts the spectral information spanning tens to hundreds of terahertz in the optical domain to a few GHz in the radio frequency (RF) domain. DCS is a powerful technique for real-time, broadband optical sampling of molecular spectra with a high signal-to-noise ratio (SNR) and tens-of-microsecond acquisition times, which requires no moving components. Avik et al. [67] demonstrated the simultaneous generation of two microresonator combs for DCS with broadband optical spectra spanning 51 THz on the same chip from a single laser, and achieved high SNR absorption spectroscopy spanning 170 nm over a 20-ms acquisition time, as shown in Figure 7(f).

Along the way, we expect that integrated OFCs will find new markets in various important applications from visible to mid-IR. In the near-IR region, silicon integrated frequency comb devices bridging the optical band and the microwave band have shown progressing mesoscopic and macroscopic applications beyond aforementioned, such as high precision spectroscopy [3, 4], sensing [9], computing [7, 8] and quantum entanglement [2]. The recently developed CMOS-foundry-based visible photonic platform leveraging wideband gap semiconductors for next generation silicon photonics [203] could possibly extend OFCs to novel wavelength ranges, such as the visible region thus bringing new opportunities in areas like atomic physics and biosensing.

3.3 Integrated quantum technologies

Quantum photonic technologies have found broad application scenarios, from communication [275] and secure key distribution [276], computing [277], to quantum metrology [278], etc. Recent advances in integrated quantum photonics [1, 279] show great promise for chip-scale quantum information processing with tremendous efficiency yet low complexity and are being intensively investigated. However, low-loss storage, transmission and computing of quantum information systems, such as trapped ions, neutral atoms, and spins in crystals are connected to photons in the UV, visible, or short near-IR bands [280]. Ultra-wideband integrated photonic devices on silicon platforms are promising candidates to enable quantum technologies.

Trapped-ion quantum (QIP) information processing [281] is among the most promising systems for quantum computing, which stores and manipulates information in atomic ions' internal and shared motional quantum states maintained in position in free space by electric fields using optical and microwave signals. Figure 8(a) shows a schematic overview of QIP. The qubits in a trapped ion quantum computer are the internal electronic states of individual atomic ions. The ions are held in an electromagnetic trap. Lasers or microwaves are used to control the qubit states $|0\rangle$ and $|1\rangle$. The internal control and the Coulomb repulsion between ions combine to form conditional logic gates. Readout is performed by measuring laser induced ion fluorescence using an auxiliary state $|a\rangle$. The laser-induced fluorescence is also used to cool the ions and prepare for quantum logic. The challenges of optical materials arise in the generation of electromagnetic traps, in the control of laser beams and in the detection of ions' fluorescence. For the typical atomic structure of the ion species used in QIP, the key requirement for optical materials is high transmittance over a wide wavelength range (0.3–2 μm) for full trapped-ion control and readout, especially the near-UV wavelengths required by many commonly used ions. In addition, the integrated photonic devices with low loss must be developed using materials that can be fabricated with low roughness, because the loss induced by Rayleigh scattering scales poorly with the decrease of wavelength. Recently, Si_3N_4 waveguides, grating couplers, with silicon dioxide cladding have been integrated into a surface-electrode trap and successfully used to deliver 674 nm light to Sr^+ ions [282], which shed blue light to other wide bandgap materials transparent from UV-to-visible wavelength range on silicon, such as Si_3N_4 [203], GaN [141], AlN [212], LN [109] and Al_2O_3 [90]. In addition to light delivery, the beams generally need to be switched on and off using

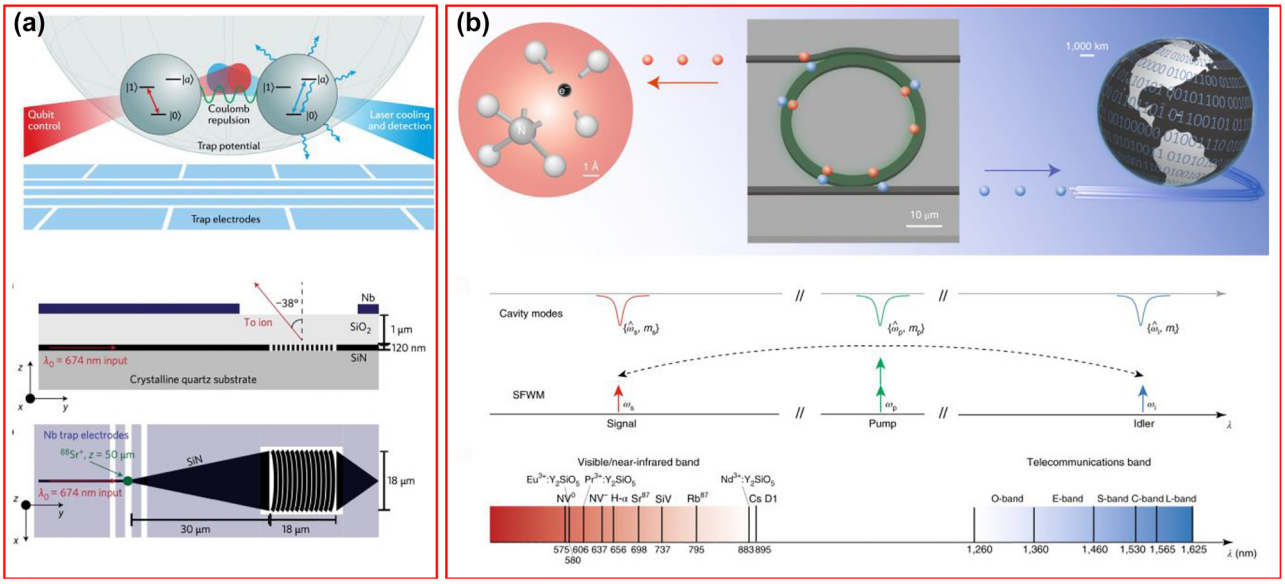

Figure 8: Integrated quantum technologies. (a) Quantum computing with trapped ions [281]; focusing grating schematic to deliver 674 nm light to Sr^+ ions [282]. (b) Chip-integrated visible–telecom entangled photon pair source for quantum communication [284]. [(a) Reproduced with permission from reference [281]. Copyright © 2021, nature publishing group; reproduced with permission from reference [282]. Copyright © 2016, nature publishing group. (b) Reproduced with permission from reference [284]. Copyright © 2019, nature publishing group].

integrated optical modulators with large EO or piezoelectric (PE) coefficients in the UV-to-visible wavelength range [279], which again can leverage the wide bandgap photonics that are transmissive over the wavelength regions of interest for trapped ions on silicon platform. Therefore, GaN [141], AlN [212] and LN [109] are the three most promising materials.

Photon pairs are the fundamental building blocks for quantum entanglement and quantum communication. Silicon photonics has demonstrated the generation of photon pairs within the telecommunications band [283]. However, the high optical attenuation of silica in the visible or short near-IR band limits the length scale of the fiber-based quantum communication between local node operations. One promising way to generate visible–telecom photon pairs is using a wide bandgap material for high Q resonators through spontaneous four-wave mixing (SFWM), as shown in Figure 8(b). Srinivasan et al. [284] have demonstrated visible–telecom time–energy entanglement in the high Q Si_3N_4 resonator with distribution over a 20-km fiber, which is far exceeding the efficient fiber length that purely visible wavelength quantum light sources can propagate. Further, using other wide bandgap materials covering visible to short near IR, such as GaN [141], AlN [212], LN [109] and Al_2O_3 [90] on silicon platform, together with the dispersion engineering of the microresonators, may enable conversion of quantum information between different species of trapped atoms/ions, defect centers, and quantum dots to the telecommunications bands for future quantum communication systems.

4 Conclusion and perspective

Although silicon photonics on SOI platform has achieved tremendous success in the telecom band, appealing platforms that support wafer-scale and heterogeneous integration of wide bandgap materials, like Si_3N_4, LN, Al_2O_3, AlN, and Ta_2O_5, are highly desired for emerging applications such as biochemical sensing and OCT [285], precise metrology and spectroscopy [3, 4], quantum optics [1, 2], RGB displays [5], atomic clocks [6], computing [7, 8], remote sensing [9], etc. These wide bandgap materials possess key performance features that are not available in SOI, including the wide transparency window from visible to mid-IR, ultralow linear, and nonlinear losses and high-power handling capability.

Here, we have reviewed some representative studies and the latest progress of these wide bandgap materials on the silicon platform. The demonstrated performance improvements are remarkable, reaching or exceeding the performance of current SOI platforms in passive, active or nonlinear applications over a wide wavelength range from visible to mid-IR. However, fully utilizing these wide bandgap materials on the silicon platform is still in the early stage of development, and we expect to see more

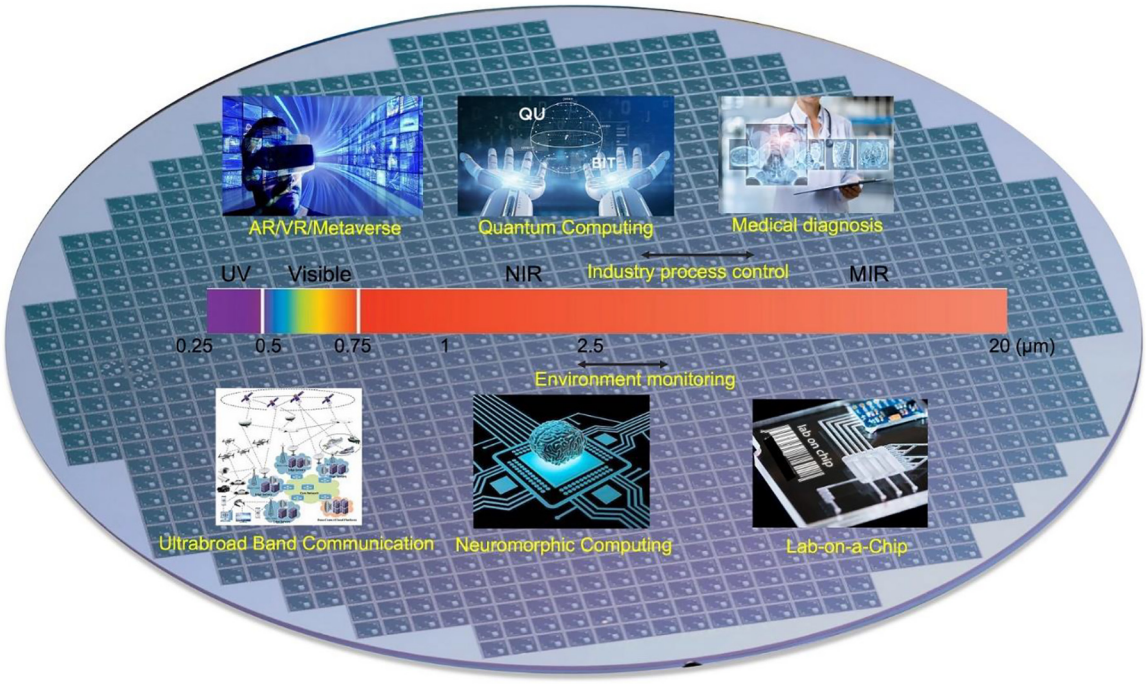

Figure 9: Future application outlook of wideband spectrum from visible to mid-IR.

developments in the future. Further work needs to reduce the waveguide loss in visible and mid-IR as they are still relatively high compared with those works reported in near-IR. Firstly, from an economic point of view, the wafer size of the wide bandgap materials on the silicon platform should be gradually increased to 8, 10, and 12 inches to allow for a large-scale fabrication. At present, only Si_3N_4 and LNOI platforms have been proved to be capable of producing large wafers. Secondly, it is still difficult to integrate electrically pumped light sources with these wide bandgap materials on silicon. III–V compound semiconductor devices are highly desired for on-chip laser sources. Substantial research has been devoted to solve this problem through hybrid/heterogeneous integration techniques [286, 287]. Thirdly, highly efficient on-chip detectors in the mid-IR range are still in the early stage. Germanium-on-silicon (or SiGe-on-Si) is a very exciting wideband material platform for detection with CMOS processing compatibility [288]. Because the direct energy gap is 0.8 eV, Ge can effectively absorb optical radiation above 1.6 μm. High-quality Ge can be epitaxially grown on silicon, and the high refractive index of Ge means that the silicon substrate can be used as the bottom cladding, which allows the transparency window to be extended to approximately 7–8 μm. In addition, Ge has a higher nonlinearity than silicon, which makes it ideal for nonlinear applications. Currently, the material quality is a challenge that hinders Ge films from achieving low losses. Finally, the integration PIC platform to fully support visible to mid-IR applications is still absent. The 3D (vertical) integration of different wide bandgap materials may be a promising route.

We believe that future technologies will cover the wide wavelength range from visible to mid-IR to address the diverse applications. Various high-performance passive, active, linear, and nonlinear components can be integrated on-chip. As shown in Figure 9, from UV to MIR, we expect to see rapid progress in the fields of ultra-broadband communication, sensing, AR/VR/Metaverse, quantum computing, neuromorphic computing, medical diagnosis, lab-on-a-chip, and so on.

Author contributions: All the authors have accepted responsibility for the entire content of this submitted manuscript and approved submission.

Research funding: This work was supported by National Key R&D Program of China (2021YFB2800404), Natural Science Foundation of China (NSFC) (62175151/61835-008/61860206001), Natural Science Foundation of Shanghai (19ZR1475400). A.D. was supported by a National Quantum Lab (Q-Lab) seed grant.

Conflict of interest statement: The authors declare no conflicts of interest regarding this article.

References

[1] H. S. Zhong, H. Wang, Y. H. Deng, et al., "Quantum computational advantage using photons," *Science*, vol. 370, p. eabe8770, 2020.

[2] K. C. Chang, X. Cheng, M. C. Sarihan, et al., "648 Hilbert-space dimensionality in a biphoton frequency comb: entanglement of formation and Schmidt mode decomposition," *Npj Quantum Inf.*, vol. 7, no. 1, p. 48, 2021.

[3] I. Coddington, N. Newbury, and W. Swann, "Dual-comb spectroscopy," *Optica*, vol. 3, no. 4, pp. 414—426, 2016.

[4] N. Picqué and T. W. Hänsch, "Frequency comb spectroscopy," *Nat. Photonics*, vol. 13, no. 3, pp. 146—157, 2019.

[5] Y. Taniyasu, M. Kasu, and T. Makimoto, "An aluminium nitride light-emitting diode with a wavelength of 210 nanometres," *Nature*, vol. 441, no. 7091, pp. 325—328, 2006.

[6] J. Vanier, "Atomic clocks based on coherent population trapping: a review," *Appl. Phys. B*, vol. 81, no. 4, pp. 421—442, 2005.

[7] X. Xu, M. Tan, B. Corcoran, et al., "11 TOPS photonic convolutional accelerator for optical neural networks," *Nature*, vol. 589, no. 7840, pp. 44—51, 2021.

[8] J. Feldmann, N. Youngblood, M. Karpov, et al., "Parallel convolutional processing using an integrated photonic tensor core," *Nature*, vol. 589, no. 7840, pp. 52—58, 2021.

[9] T. Tan, Z. Yuan, H. Zhang, et al., "Multispecies and individual gas molecule detection using Stokes solitons in a graphene over-modal microresonator," *Nat. Commun.*, vol. 12, no. 1, p. 6716, 2021.

[10] B. J. Eggleton, B. Luther-Davies, and K. Richardson, "Chalcogenide photonics," *Nat. Photonics*, vol. 5, no. 3, pp. 141—148, 2011.

[11] B. Shen, H. Lin, F. Merget, et al., "Broadband couplers for hybrid silicon-chalcogenide glass photonic integrated circuits," *Opt. Express*, vol. 27, no. 10, pp. 13781—13792, 2019.

[12] H. Lin, Y. Song, Y. Huang, et al., "Chalcogenide glass-on-graphene photonics," *Nat. Photonics*, vol. 11, no. 12, pp. 798—805, 2017.

[13] J. M. Ramirez, Q. Liu, V. Vakarin, et al., "Graded SiGe waveguides with broadband low-loss propagation in the mid infrared," *Opt. Express*, vol. 26, no. 2, pp. 870—877, 2018.

[14] R. Soref, "Mid-infrared photonics in silicon and germanium," *Nat. Photonics*, vol. 4, pp. 495—497, 2010.

[15] Y. Su, Y. Zhang, C. Qiu, X. Guo, and L. Sun, "Silicon photonic platform for passive waveguide devices: materials, fabrication, and applications," *Adv. Mater. Technol.*, vol. 5, no. 8, p. 1901153, 2020.

[16] V. M. Lavchiev and B. Jakoby, "Photonics in the mid-infrared: challenges in single-chip integration and absorption sensing," *IEEE J. Sel. Top. Quantum Electron.*, vol. 23, no. 2, pp. 452—463, 2017.

[17] D. J. Blumenthal, "Photonic integration for UV to IR applications," *APL Photonics*, vol. 5, no. 2, p. 020903, 2020.

[18] A. Himeno, K. Kato, and T. Miya, "Silica-based planar lightwave circuits," *IEEE J. Sel. Top. Quantum Electron.*, vol. 4, no. 6, pp. 913—924, 1998.

[19] K. Ikeda, R. E. Saperstein, N. Alic, and Y. Fainman, "Thermal and Kerr nonlinear properties of plasma-deposited silicon nitride/silicon dioxide waveguides," *Opt. Express*, vol. 16, no. 17, pp. 12987—12994, 2008.

[20] A. Boskovic, L. Gruner-Nielsen, O. A. Levring, S. V. Chernikov, and J. R. Taylor, "Direct continuous-wave measurement of n2 in various types of telecommunication fiber at 1.55 μm," *Opt. Lett.*, vol. 21, no. 24, pp. 1966—1968, 1996.

[21] B. Dong, X. Guo, C. P. Ho, et al., "Silicon-on-Insulator waveguide devices for broadband mid-infrared photonics," *IEEE Photon. J.*, vol. 9, no. 3, pp. 1—10, 2017.

[22] Y. Zhang, Y. He, Q. Zhu, et al., "Single-resonance silicon nanobeam filter with an ultra-high thermo-optic tuning efficiency over a wide continuous tuning range," *Opt. Lett.*, vol. 43, no. 18, pp. 4518—4521, 2018.

[23] Q. Xu, B. Schmidt, S. Pradhan, and M. Lipson, "Micrometre-scale silicon electro-optic modulator," *Nature*, vol. 435, pp. 325—327, 2005.

[24] F. Xia, L. Sekaric, and Y. Vlasov, "Ultracompact optical buffers on a silicon chip," *Nat. Photonics*, vol. 1, no. 1, pp. 65—71, 2007.

[25] Y. Su and Y. Zhang, *Passive Silicon Photonic Devices*, Melville, New York, (AIP Publishing Books), AIP Publishing LLC, 2022, p. 188.

[26] D. Thomson, A. Zilkie, J. E. Bowers, et al., "Roadmap on silicon photonics," *J. Opt.*, vol. 18, no. 7, p. 073003, 2016.

[27] Intel®, *Intel® Silicon Photonics 100G PSM4 QSFP28 Optical Transceiver*, 2016 [Online]. Available at: https://ark.intel.com/content/www/us/en/ark/products/96610/intel-silicon-photonics-100g-psm4-qsfp28-optical-transceiver.html.

[28] G. T. Reed, G. Mashanovich, F. Y. Gardes, and D. J. Thomson, "Silicon optical modulators," *Nat. Photonics*, vol. 4, no. 8, pp. 518—526, 2010.

[29] Y. Zhao, J. Xiang, Y. He, et al., "On-chip metamaterial enabled wavelength (de)multiplexer," *Laser Photon. Rev.*, vol. 16, no. 7, p. 2200005, 2022.

[30] M. Casalino, G. Coppola, R. M. De La Rue, and D. F. Logan, "State-of-the-art all-silicon sub-bandgap photodetectors at telecom and datacom wavelengths," *Laser Photon. Rev.*, vol. 10, no. 6, pp. 895—921, 2016.

[31] Z. Cheng, Y. Zhao, J. Zhang, et al., "Generalized modular spectrometers combining a compact nanobeam microcavity and computational reconstruction," *ACS Photonics*, vol. 9, no. 1, pp. 74—81, 2022.

[32] Y. Shen, N. C. Harris, S. Skirlo, et al., "Deep learning with coherent nanophotonic circuits," *Nat. Photonics*, vol. 11, no. 7, pp. 441—446, 2017.

[33] X. Guo, J. Xiang, Y. Zhang, and Y. Su, "Integrated neuromorphic photonics: synapses, neurons, and neural networks," *Adv. photonics Res.*, vol. 2, no. 6, p. 2000212, 2021.

[34] E. Timurdogan, C. V. Poulton, M. J. Byrd, and M. R. Watts, "Electric field-induced second-order nonlinear optical effects in silicon waveguides," *Nat. Photonics*, vol. 11, no. 3, pp. 200—206, 2017.

[35] S. Y. Siew, B. Li, F. Gao, et al., "Review of silicon photonics technology and platform development," *J. Lightwave Technol.*, vol. 39, no. 13, pp. 4374—4389, 2021.

[36] Y. Zou, S. Chakravarty, C. J. Chung, X. Xu, and R. T. Chen, "Mid-infrared silicon photonic waveguides and devices [invited]," *Photonics Res.*, vol. 6, no. 4, pp. 254—276, 2018.

[37] S. A. Miller, M. Yu, X. Ji, et al., "Low-loss silicon platform for broadband mid-infrared photonics," *Optica*, vol. 4, no. 7, pp. 707—712, 2017.

[38] J. Leuthold, C. Koos, and W. Freude, "Nonlinear silicon photonics," *Nat. Photonics*, vol. 4, no. 8, pp. 535—544, 2010.
[39] Z. Cheng, X. Chen, C. Y. Wong, K. Xu, and H. K. Tsang, "Mid-infrared suspended membrane waveguide and ring resonator on silicon-on-insulator," *IEEE Photon. J.*, vol. 4, no. 5, pp. 1510—1519, 2012.
[40] Z. Cheng, X. Chen, C. Y. Wong, et al., "Focusing subwavelength grating coupler for mid-infrared suspended membrane waveguide," *Opt. Lett.*, vol. 37, no. 7, pp. 1217—1219, 2012.
[41] M. S. Rouifed, C. G. Littlejohns, G. X. Tina, et al., "Ultra-compact MMI-based beam splitter demultiplexer for the NIR/MIR wavelengths of 1.55 μm and 2 μm," *Opt. Express*, vol. 25, no. 10, pp. 10893—10900, 2017.
[42] M. Nedeljkovic, S. Stankovic, C. J. Mitchell, et al., "Mid-infrared thermo-optic modulators in SoI," *IEEE Photon. Technol. Lett.*, vol. 26, no. 13, pp. 1352—1355, 2014.
[43] M. A. Van Camp, S. Assefa, D. M. Gill, et al., "Demonstration of electrooptic modulation at 2165 nm using a silicon Mach—Zehnder interferometer," *Opt. Express*, vol. 20, no. 27, pp. 28009—28016, 2012.
[44] A. G. Griffith, R. K. Lau, J. Cardenas, et al., "Silicon-chip mid-infrared frequency comb generation," *Nat. Commun.*, vol. 6, no. 1, p. 6299, 2015.
[45] B. Kuyken, T. Ideguchi, S. Holzner, et al., "An octave-spanning mid-infrared frequency comb generated in a silicon nanophotonic wire waveguide," *Nat. Commun.*, vol. 6, p. 6310, 2015.
[46] E. Shim, A. Gil-Molina, O. Westreich, et al., "Tunable single-mode chip-scale mid-infrared laser," *Commun. Phys.*, vol. 4, no. 1, p. 268, 2021.
[47] X. Liu, R. M. Osgood, Y. A. Vlasov, and W. M. J. Green, "Mid-infrared optical parametric amplifier using silicon nanophotonic waveguides," *Nat. Photonics*, vol. 4, no. 8, pp. 557—560, 2010.
[48] B. Kuyken, X. Liu, R. M. Osgood, et al., "Frequency conversion of mid-infrared optical signals into the telecom band using nonlinear silicon nanophotonic wires," in *Optical Fiber Communication Conference/National Fiber Optic Engineers Conference 2011*, Los Angeles, California, Optica Publishing Group, in OSA Technical Digest (CD), 2011, p. OThU4.
[49] X. Ji, S. Roberts, M. Corato-Zanarella, and M. Lipson, "Methods to achieve ultra-high quality factor silicon nitride resonators," *APL Photonics*, vol. 6, no. 7, p. 071101, 2021.
[50] X. Ji, F. A. S. Barbosa, S. P. Roberts, et al., "Ultra-low-loss on-chip resonators with sub-milliwatt parametric oscillation threshold," *Optica*, vol. 4, no. 6, pp. 619—624, 2017.
[51] J. S. Levy, A. Gondarenko, M. A. Foster, A. C. Turner-Foster, A. L. Gaeta, and M. Lipson, "CMOS-compatible multiple-wavelength oscillator for on-chip optical interconnects," *Nat. Photonics*, vol. 4, no. 1, pp. 37—40, 2009.
[52] A. Mohanty, Q. Li, M. A. Tadayon, et al., "Reconfigurable nanophotonic silicon probes for sub-millisecond deep-brain optical stimulation," *Nat. Biomed. Eng.*, vol. 4, no. 2, pp. 223—231, 2020.
[53] A. Frigg, A. Boes, G. Ren, et al., "Low loss CMOS-compatible silicon nitride photonics utilizing reactive sputtered thin films," *Opt. Express*, vol. 27, no. 26, p. 37795, 2019.
[54] J. T. Boyd and C. S. Kuo, "Composite prism—grating coupler for coupling light into high refractive index thin-film waveguides," *Appl. Opt.*, vol. 15, no. 7, pp. 1681—1683, 1976.
[55] W. Stutius and W. Streifer, "Silicon nitride films on silicon for optical waveguides," *Appl. Opt.*, vol. 16, no. 12, pp. 3218—3222, 1977.
[56] M. J. Shaw, J. Guo, G. A. Vawter, S. Habermehl, and C. T. Sullivan, "Fabrication techniques for low-loss silicon nitride waveguides," in *MOEMS-MEMS Micro & Nanofabrication*, vol. 5720, E. G. Johnson, G. P. Nordin, and T. J. Suleski, Eds., San Jose, CA, SPIE, 2005.
[57] D. T. Spencer, J. F. Bauters, M. J. R. Heck, and J. E. Bowers, "Integrated waveguide coupled Si_3N_4 resonators in the ultrahigh-Q regime," *Optica*, vol. 1, no. 3, p. 153, 2014.
[58] Y. Xuan, Y. Liu, L. T. Varghese, et al., "High-Q silicon nitride microresonators exhibiting low-power frequency comb initiation," *Optica*, vol. 3, no. 11, pp. 1171—1180, 2016.
[59] M. H. P. Pfeiffer, J. Liu, A. S. Raja, T. Morais, B. Ghadiani, and T. J. Kippenberg, "Ultra-smooth silicon nitride waveguides based on the Damascene reflow process: fabrication and loss origins," *Optica*, vol. 5, no. 7, pp. 884—892, 2018.
[60] M. H. P. Pfeiffer, C. Herkommer, J. Liu, et al., "Photonic damascene process for low-loss, high-confinement silicon nitride waveguides," *IEEE J. Sel. Top. Quantum Electron.*, vol. 24, no. 4, pp. 1—11, 2018.
[61] B. Stern, X. Ji, Y. Okawachi, A. L. Gaeta, and M. Lipson, "Battery-operated integrated frequency comb generator," *Nature*, vol. 562, no. 7727, pp. 401—405, 2018.
[62] G. Yurtsever, B. Považay, A. Alex, B. Zabihian, W. Drexler, and R. Baets, "Photonic integrated Mach—Zehnder interferometer with an on-chip reference arm for optical coherence tomography," *Biomed. Opt. Express*, vol. 5, no. 4, p. 1050, 2014.
[63] X. Ji, X. Yao, A. Klenner, et al., "Chip-based frequency comb sources for optical coherence tomography," *Opt. Express*, vol. 27, no. 14, pp. 19896—19905, 2019.
[64] J. Pfeifle, V. Brasch, M. Lauermann, et al., "Coherent terabit communications with microresonator Kerr frequency combs," *Nat. Photonics*, vol. 8, no. 5, pp. 375—380, 2014.
[65] A. Fülöp, M. Mazur, A. Lorences-Riesgo, et al., "High-order coherent communications using mode-locked dark-pulse Kerr combs from microresonators," *Nat. Commun.*, vol. 9, no. 1, p. 1598, 2018.
[66] B. Y. Kim, Y. Okawachi, J. K. Jang, et al., "Turn-key, high-efficiency Kerr comb source," *Opt. Lett.*, vol. 44, no. 18, pp. 4475—4478, 2019.
[67] A. Dutt, C. Joshi, X. Ji, et al., "On-chip dual-comb source for spectroscopy," *Sci. Adv.*, vol. 4, no. 3, p. e1701858, 2018.
[68] M. Yu, Y. Okawachi, C. Joshi, X. Ji, M. Lipson, and A. L. Gaeta, "Gas-phase microresonator-based comb spectroscopy without an external pump laser," *ACS Photonics*, vol. 5, no. 7, pp. 2780—2785, 2018.
[69] P. Trocha, M. Karpov, D. Ganin, et al., "Ultrafast optical ranging using microresonator soliton frequency combs," *Science*, vol. 359, no. 6378, pp. 887—891, 2018.
[70] P. Muellner, E. Melnik, G. Koppitsch, J. Kraft, F. Schrank, and R. Hainberger, "CMOS-Compatible Si 3 N 4 waveguides for optical biosensing," *Procedia Eng.*, vol. 120, pp. 578—581, 2015.
[71] T. Taniguchi, A. Hirowatari, T. Ikeda, et al., "Detection of antibody-antigen reaction by silicon nitride slot-ring biosensors using protein G," *Opt. Commun.*, vol. 365, pp. 16—23, 2016.

[72] C. Schuck, W. H. P. Pernice, and H. X. Tang, "NbTiN superconducting nanowire detectors for visible and telecom wavelengths single photon counting on Si_3N_4 photonic circuits," *Appl. Phys. Lett.*, vol. 102, no. 5, p. 051101, 2013.
[73] C. Taballione, T. A. W. Wolterink, J. Lugani, et al., "8 × 8 reconfigurable quantum photonic processor based on silicon nitride waveguides," *Opt. Express*, vol. 27, no. 19, pp. 26842—26857, 2019.
[74] C. Joshi, A. Farsi, A. Dutt, et al., "Frequency-domain quantum interference with correlated photons from an integrated microresonator," *Phys. Rev. Lett.*, vol. 124, no. 14, p. 143601, 2020.
[75] Y. Zhao, Y. Okawachi, J. K. Jang, X. Ji, M. Lipson, and A. L. Gaeta, "Near-degenerate quadrature-squeezed vacuum generation on a silicon-nitride chip," *Phys. Rev. Lett.*, vol. 124, no. 19, p. 193601, 2020.
[76] C. Xiang, M. L. Davenport, J. B. Khurgin, P. A. Morton, and J. E. Bowers, "Low-loss continuously tunable optical true time delay based on Si_3N_4 ring resonators," *IEEE J. Sel. Top. Quantum Electron.*, vol. 24, no. 4, pp. 1—9, 2018.
[77] Z. L. Newman, V. Maurice, T. Drake, et al., "Architecture for the photonic integration of an optical atomic clock," *Optica*, vol. 6, no. 5, pp. 680—685, 2019.
[78] C. V. Poulton, M. J. Byrd, M. Raval, et al., "Large-scale silicon nitride nanophotonic phased arrays at infrared and visible wavelengths," *Opt. Lett.*, vol. 42, no. 1, pp. 21—24, 2017.
[79] M. Chul Shin, A. Mohanty, K. Watson, et al., "Chip-scale blue light phased array," *Opt. Lett.*, vol. 45, no. 7, pp. 1934—1937, 2020.
[80] R. M. Oldenbeuving, E. J. Klein, H. L. Offerhaus, C. J. Lee, H. Song, and K. J. Boller, "25 kHz narrow spectral bandwidth of a wavelength tunable diode laser with a short waveguide-based external cavity," *Laser Phys. Lett.*, vol. 10, no. 1, p. 015804, 2012.
[81] D. T. Spencer, M. L. Davenport, T. Komljenovic, S. Srinivasan, and J. E. Bowers, "Stabilization of heterogeneous silicon lasers using Pound—Drever—Hall locking to Si_3N_4 ring resonators," *Opt. Express*, vol. 24, no. 12, pp. 13511—13517, 2016.
[82] Y. Fan, J. P. Epping, R. M. Oldenbeuving, et al., "Optically integrated InP—Si_3N_4 hybrid laser," *IEEE Photon. J.*, vol. 8, no. 6, pp. 1—11, 2016.
[83] B. Stern, X. Ji, A. Dutt, and M. Lipson, "Compact narrow-linewidth integrated laser based on a low-loss silicon nitride ring resonator," *Opt. Lett.*, vol. 42, no. 21, p. 4541, 2017.
[84] C. Xiang, W. Jin, J. Guo, et al., "Narrow-linewidth III-V/Si/Si_3N_4 laser using multilayer heterogeneous integration," *Optica*, vol. 7, no. 1, pp. 20—21, 2020.
[85] A. Gil-Molina, O. Westreich, Y. Antman, X. Ji, A. L. Gaeta, and M. Lipson, "Robust hybrid III-V/Si_3N_4 laser with kHz-linewidth and GHz-pulling range," in *2020 Conference on Lasers and Electro-Optics (CLEO)*, 2020, pp. 1—2.
[86] B. Shen, L. Chang, J. Liu, et al., "Integrated turnkey soliton microcombs," *Nature*, vol. 582, no. 7812, pp. 365—369, 2020.
[87] H. Lee, T. Chen, J. Li, O. Painter, and K. J. Vahala, "Ultra-low-loss optical delay line on a silicon chip," *Nat. Commun.*, vol. 3, no. 1, p. 867, 2012.
[88] H. Lee, T. Chen, J. Li, et al., "Chemically etched ultrahigh-Q wedge-resonator on a silicon chip," *Nat. Photonics*, vol. 6, no. 6, pp. 369—373, 2012.
[89] D. J. Moss, R. Morandotti, A. L. Gaeta, and M. Lipson, "New CMOS-compatible platforms based on silicon nitride and Hydex for nonlinear optics," *Nat. Photonics*, vol. 7, no. 8, pp. 597—607, 2013.
[90] G. West, *Seeing Blue: Pushing Integrated Photonics into the Ultraviolet with ALD Aluminum Oxide (SPIE OPTO)*, San Francisco, California, SPIE, 2020.
[91] H. Jung, S. P. Yu, D. R. Carlson, T. E. Drake, T. C. Briles, and S. B. Papp, "Tantala Kerr nonlinear integrated photonics," *Optica*, vol. 8, no. 6, pp. 811—817, 2021.
[92] U. Tisch, B. Meyler, O. Katz, E. Finkman, and J. Salzman, "Dependence of the refractive index of $Al_xGa_{1-x}N$ on temperature and composition at elevated temperatures," *J. Appl. Phys.*, vol. 89, no. 5, pp. 2676—2685, 2001.
[93] N. Watanabe, T. Kimoto, and J. Suda, "Thermo-optic coefficients of 4H-SiC, GaN, and AlN for ultraviolet to infrared regions up to 500 $^{\circ}$C," *Jpn. J. Appl. Phys.*, vol. 51, p. 112101, 2012.
[94] D. Munk, M. Katzman, O. Westreich, et al., "Four-wave mixing and nonlinear parameter measurement in a gallium-nitride ridge waveguide," *Opt. Mater. Express*, vol. 8, no. 1, p. 66, 2018.
[95] E. Stassen, M. Pu, E. Semenova, E. Zavarin, W. Lundin, and K. Yvind, "High-confinement gallium nitride-on-sapphire waveguides for integrated nonlinear photonics," *Opt. Lett.*, vol. 44, no. 5, p. 1064, 2019.
[96] S. Abel, F. Eltes, J. E. Ortmann, et al., "Large Pockels effect in micro- and nanostructured barium titanate integrated on silicon," *Nat. Mater.*, vol. 18, pp. 42—47, 2019.
[97] C. Sorace-Agaskar, D. Kharas, S. Yegnanarayanan, et al., "Versatile silicon nitride and alumina integrated photonic platforms for the ultraviolet to short-wave infrared," *IEEE J. Sel. Top. Quantum Electron.*, vol. 25, no. 5, pp. 1—15, 2019.
[98] M. M. Aslan, N. A. Webster, C. L. Byard, et al., "Low-loss optical waveguides for the near ultra-violet and visible spectral regions with Al_2O_3 thin films from atomic layer deposition," *Thin Solid Films*, vol. 518, no. 17, pp. 4935—4940, 2010.
[99] M. Belt, M. L. Davenport, J. E. Bowers, and D. J. Blumenthal, "Ultra-low-loss Ta_2O_5-core/SiO_2-clad planar waveguides on Si substrates," *Optica*, vol. 4, no. 5, pp. 532—536, 2017.
[100] R. Y. Chen, M. D. Charlton, and P. G. Lagoudakis, "Chi 3 dispersion in planar tantalum pentoxide waveguides in the telecommunications window," *Opt. Lett.*, vol. 34, no. 7, pp. 1135—1137, 2009.
[101] C. L. Wu, Y. J. Chiu, C. L. Chen, Y. Y. Lin, A. K. Chu, and C. K. Lee, "Four-wave-mixing in the loss low submicrometer Ta_2O_5 channel waveguide," *Opt. Lett.*, vol. 40, no. 19, pp. 4528—4531, 2015.
[102] A. Raza, S. Clemmen, P. Wuytens, et al., "High index contrast photonic platforms for on-chip Raman spectroscopy," *Opt. Express*, vol. 27, no. 16, pp. 23067—23079, 2019.
[103] D. A. Coucheron, O. I. Helle, J. S. Wilkinson, et al., "Study of waveguide background at visible wavelengths for on-chip nanoscopy," *Opt. Express*, vol. 29, no. 13, pp. 20735—20746, 2021.
[104] E. L. Wooten, K. Kissa, A. Yi-Yan, et al., "A review of lithium niobate modulators for fiber-optic communications systems," *IEEE J. Sel. Top. Quantum Electron.*, vol. 6, no. 1, pp. 69—82, 2000.
[105] A. Boes, B. Corcoran, L. Chang, J. Bowers, and A. Mitchell, "Status and potential of lithium niobate on insulator (LNOI) for photonic integrated circuits," *Laser Photon. Rev.*, vol. 12, no. 4, p. 1700256, 2018.
[106] Y. Qi and Y. Li, "Integrated lithium niobate photonics," *Nanophotonics*, vol. 9, no. 6, pp. 1287—1320, 2020.

[107] H. Hu, R. Ricken, W. Sohler, and R. B. Wehrspohn, "Lithium niobate ridge waveguides fabricated by wet etching," *IEEE Photon. Technol. Lett.*, vol. 19, no. 6, pp. 417–419, 2007.
[108] M. Wang, R. Wu, J. Lin, et al., "Chemo-mechanical polish lithography: a pathway to low loss large-scale photonic integration on lithium niobate on insulator," *Quantum Eng.*, vol. 1, no. 1, p. e9, 2019.
[109] M. Zhang, C. Wang, R. Cheng, A. Shams-Ansari, and M. Lončar, "Monolithic ultra-high-Q lithium niobate microring resonator," *Optica*, vol. 4, no. 12, pp. 1536–1537, 2017.
[110] B. Desiatov, A. Shams-Ansari, M. Zhang, C. Wang, and M. Lončar, "Ultra-low-loss integrated visible photonics using thin-film lithium niobate," *Optica*, vol. 6, no. 3, pp. 380–384, 2019.
[111] T. Ren, M. Zhang, C. Wang, et al., "An integrated low-voltage broadband lithium niobate phase modulator," *IEEE Photon. Technol. Lett.*, vol. 31, no. 11, pp. 889–892, 2019.
[112] C. Wang, M. Zhang, X. Chen, et al., "Integrated lithium niobate electro-optic modulators operating at CMOS-compatible voltages," *Nature*, vol. 562, no. 7725, pp. 101–104, 2018.
[113] D. Zhu, L. Shao, M. Yu, et al., "Integrated photonics on thin-film lithium niobate," *Adv. Opt. Photonics*, vol. 13, no. 2, pp. 242–352, 2021.
[114] M. Yu, L. Shao, Y. Okawachi, A. L. Gaeta, and M. Loncar, "Ultraviolet to mid-infrared supercontinuum generation in lithium-niobate waveguides," in *Conference on Lasers and Electro-Optics*, Washington, DC, Optica Publishing Group, in OSA Technical Digest, 2020, p. STu4H.1.
[115] R. B. Karabalin, M. H. Matheny, X. L. Feng, et al., "Piezoelectric nanoelectromechanical resonators based on aluminum nitride thin films," *Appl. Phys. Lett.*, vol. 95, no. 10, p. 103111, 2009.
[116] N. Sinha, G. E. Wabiszewski, R. Mahameed, et al., "Piezoelectric aluminum nitride nanoelectromechanical actuators," *Appl. Phys. Lett.*, vol. 95, no. 5, p. 053106, 2009.
[117] W. H. P. Pernice, C. Xiong, and H. X. Tang, "High Q micro-ring resonators fabricated from polycrystalline aluminum nitride films for near infrared and visible photonics," *Opt. Express*, vol. 20, no. 11, pp. 12261–12269, 2012.
[118] P. T. Lin, H. Jung, L. C. Kimerling, A. Agarwal, and H. X. Tang, "Low-loss aluminium nitride thin film for mid-infrared microphotonics," *Laser Photon. Rev.*, vol. 8, no. 2, pp. L23–L28, 2014.
[119] B. Dong, X. Luo, S. Zhu, et al., "Aluminum nitride on insulator (AlNOI) platform for mid-infrared photonics," *Opt. Lett.*, vol. 44, no. 1, pp. 73–76, 2019.
[120] P. Gräupner, J. C. Pommier, A. Cachard, and J. L. Coutaz, "Electro-optical effect in aluminum nitride waveguides," *J. Appl. Phys.*, vol. 71, no. 9, pp. 4136–4139, 1992.
[121] C. Xiong, W. H. P. Pernice, and H. X. Tang, "Low-loss, silicon integrated, aluminum nitride photonic circuits and their use for electro-optic signal processing," *Nano Lett.*, vol. 12, no. 7, pp. 3562–3568, 2012.
[122] S. Zhu and G. Q. Lo, "Aluminum nitride electro-optic phase shifter for backend integration on silicon," *Opt. Express*, vol. 24, no. 12, pp. 12501–12506, 2016.
[123] K. Tsubouchi and N. Mikoshiba, "Zero-temperature-coefficient SAW devices on AlN epitaxial films," *IEEE Trans. Son. Ultrason.*, vol. 32, pp. 634–644, 1985.
[124] A. Sanz-Hervás, M. Clement, E. Iborra, L. Vergara, J. Olivares, and J. Sangrador, "Degradation of the piezoelectric response of sputtered c-axis AlN thin films with traces of non-(0002) x-ray diffraction peaks," *Appl. Phys. Lett.*, vol. 88, no. 16, p. 161915, 2006.
[125] S. A. Tadesse and M. Li, "Sub-optical wavelength acoustic wave modulation of integrated photonic resonators at microwave frequencies," *Nat. Commun.*, vol. 5, no. 1, p. 5402, 2014.
[126] C. Xiong, X. Sun, K. Y. Fong, and H. X. Tang, "Integrated high frequency aluminum nitride optomechanical resonators," *Appl. Phys. Lett.*, vol. 100, no. 17, p. 171111, 2012.
[127] S. Y. Davydov, "Evaluation of physical parameters for the group III nitrates: BN, AlN, GaN, and InN," *Semiconductors*, vol. 36, no. 1, pp. 41–44, 2002.
[128] H. Li, S. A. Tadesse, Q. Liu, and M. Li, "Nanophotonic cavity optomechanics with propagating acoustic waves at frequencies up to 12 GHz," *Optica*, vol. 2, no. 9, pp. 826–831, 2015.
[129] E. Crisman, A. Drehman, R. Miller, A. Osinsky, D. Volovik, and V. Vasilyev, "Enhanced AlN nanostructures for pyroelectric sensors," *Phys. Status Solidi C*, vol. 11, nos. 3–4, pp. 517–520, 2014.
[130] C. Ranacher, C. Consani, A. Tortschanoff, et al., "A CMOS compatible pyroelectric mid-infrared detector based on aluminium nitride," *Sensors*, vol. 19, no. 11, p. 2513, 2019.
[131] J. W. Stewart, J. H. Vella, W. Li, S. Fan, and M. H. Mikkelsen, "Ultrafast pyroelectric photodetection with on-chip spectral filters," *Nat. Mater.*, vol. 19, no. 2, pp. 158–162, 2020.
[132] D. K. T. Ng, G. Wu, T. T. Zhang, et al., "Considerations for an 8-inch wafer-level CMOS compatible AlN pyroelectric 5–14 μm wavelength IR detector towards miniature integrated photonics gas sensors," *J. Microelectromech. Syst.*, vol. 29, no. 5, pp. 1199–1207, 2020.
[133] X. Liu, C. Sun, B. Xiong, et al., "Aluminum nitride-on-sapphire platform for integrated high-Q microresonators," *Opt. Express*, vol. 25, no. 2, p. 587, 2017.
[134] Y. Sun, W. Shin, D. A. Laleyan, et al., "Ultrahigh Q microring resonators using a single-crystal aluminum-nitride-on-sapphire platform," *Opt. Lett.*, vol. 44, no. 23, pp. 5679–5682, 2019.
[135] S. Nakamura, S. Pearton, and G. Fasol, *The Blue Laser Diode: The Complete Story*, Berlin, Heidelberg, Springer Berlin Heidelberg, 2000.
[136] S. Nakamura, M. Senoh, and T. Mukai, "High-power InGaN/GaN double-heterostructure violet light emitting diodes," *Appl. Phys. Lett.*, vol. 62, no. 19, pp. 2390–2392, 1993.
[137] A. Chowdhury, H. M. Ng, M. Bhardwaj, and N. G. Weimann, "Second-harmonic generation in periodically poled GaN," *Appl. Phys. Lett.*, vol. 83, no. 6, pp. 1077–1079, 2003.
[138] S. N. Mohammad, A. A. Salvador, and H. Morkoc, "Emerging gallium nitride based devices," *Proc. IEEE*, vol. 83, no. 10, pp. 1306–1355, 1995.
[139] H. C. Chiamori, M. Hou, C. A. Chapin, A. Shankar, and D. G. Senesky, "Characterization of gallium nitride microsystems within radiation and high-temperature environments," in *SPIE MOEMS-MEMS*, H. R. Shea, and R. Ramesham, Eds., San Francisco, California, United States, 2014, p. 897507.
[140] S. R. Bowman, C. G. Brown, and B. Taczak, "Optical dispersion and phase matching in gallium nitride and aluminum nitride," *Opt. Mater. Express*, vol. 8, no. 4, p. 1091, 2018.

[141] C. Xiong, W. Pernice, K. K. Ryu, et al., "Integrated GaN photonic circuits on silicon (100) for second harmonic generation," *Opt. Express*, vol. 19, no. 11, p. 10462, 2011.
[142] S. Nakamura, "Nobel Lecture: background story of the invention of efficient blue InGaN light emitting diodes," *Rev. Mod. Phys.*, vol. 87, no. 4, pp. 1139—1151, 2015.
[143] J. Li, J. Y. Lin, and H. X. Jiang, "Growth of III-nitride photonic structures on large area silicon substrates," *Appl. Phys. Lett.*, vol. 88, no. 17, p. 171909, 2006.
[144] D. Zhu, D. J. Wallis, and C. J. Humphreys, "Prospects of III-nitride optoelectronics grown on Si," *Rep. Prog. Phys.*, vol. 76, no. 10, p. 106501, 2013.
[145] O. Westreich, M. Katz, Y. Paltiel, O. Ternyak, and N. Sicron, "Low propagation loss in GaN/AlGaN-based ridge waveguides: low propagation loss in GaN/AlGaN-based ridge waveguides," *Phys. Status Solidi A*, vol. 212, no. 5, pp. 1043—1048, 2015.
[146] Y. Zhang, L. McKnight, E. Engin, et al., "GaN directional couplers for integrated quantum photonics," *Appl. Phys. Lett.*, vol. 99, no. 16, p. 161119, 2011.
[147] J. Hite, M. Twigg, M. Mastro, et al., "Development of periodically oriented gallium nitride for non-linear optics [invited]," *Opt. Mater. Express*, vol. 2, no. 9, p. 1203, 2012.
[148] S. Sakr, P. Crozat, D. Gacemi, et al., "GaN/AlGaN waveguide quantum cascade photodetectors at $\lambda \approx 1.55$ μm with enhanced responsivity and -40 GHz frequency bandwidth," *Appl. Phys. Lett.*, vol. 102, no. 1, p. 011135, 2013.
[149] Y. Zheng, C. Sun, B. Xiong, et al., "Integrated gallium nitride nonlinear photonics," *Laser Photon. Rev.*, vol. 16, no. 1, p. 2100071, 2022.
[150] H. Chen, H. Fu, X. Huang, et al., "Low loss GaN waveguides at the visible spectral wavelengths for integrated photonics applications," *Opt. Express*, vol. 25, no. 25, p. 31758, 2017.
[151] M. Gromovyi, M. El Kurdi, X. Checoury, et al., "Low-loss GaN-on-insulator platform for integrated photonics," *Opt. Express*, vol. 30, no. 12, p. 20737, 2022.
[152] X. C. Long, R. A. Myers, S. R. J. Brueck, R. Ramer, K. Zheng, and S. D. Hersee, "GaN linear electro-optic effect," *Appl. Phys. Lett.*, vol. 67, no. 10, pp. 1349—1351, 1995.
[153] O. Westreich, G. Atar, Y. Paltiel, and N. Sicron, "Reducing optical losses in GaN waveguides — toward an electro-optic phase modulator," *Phys. Status Solidi A*, vol. 215, no. 9, p. 1700551, 2018.
[154] A. Stolz, L. Considine, E. Dogheche, D. Decoster, and D. Pavlidis, "Prospective for gallium nitride-based optical waveguide modulators," *IEICE Trans. Electron. C*, vol. E958, pp. 1363—1368, 2012., no.
[155] A. Petraru, J. Schubert, M. Schmid, O. Trithaveesak, and C. Buchal, "Integrated optical Mach Zehnder modulator based on polycrystalline $BaTiO_3$," *Opt. Lett.*, vol. 28, no. 24, pp. 2527—2529, 2003.
[156] A. Petraru, J. Schubert, M. Schmid, and C. Buchal, "Ferroelectric $BaTiO_3$ thin-film optical waveguide modulators," *Appl. Phys. Lett.*, vol. 81, no. 8, pp. 1375—1377, 2002.
[157] P. Girouard, P. Chen, Y. K. Jeong, Z. Liu, S. T. Ho, and B. W. Wessels, "X(2) modulator with 40-GHz modulation utilizing $BaTiO_3$ photonic crystal waveguides," *IEEE J. Quantum Electron.*, vol. 53, no. 4, pp. 1—10, 2017.
[158] L. Czornomaz and S. Abel, "BTO-enhanced silicon photonics — a scalable PIC platform with ultra-efficient electro-optical modulation," in *Optical Fiber Communication Conference (OFC) 2022*, S. P. D. S. W. J. F. C. R. R. Matsuo, and D. Simeonidou, Eds., San Diego, California, Optica Publishing Group, in Technical Digest Series, 2022, p. Th1J.1.
[159] F. Eltes, G. E. Villarreal-Garcia, D. Caimi, et al., "An integrated optical modulator operating at cryogenic temperatures," *Nat. Mater.*, vol. 19, pp. 1—5, 2020.
[160] J. Geler-Kremer, F. Eltes, P. Stark, et al., "A non-volatile optical memory in silicon photonics," in *Optical Fiber Communication Conference (OFC) 2021*, P. K. J. X. C. C. R. C. C. Dong, and M. Li, Eds., Washington, DC, Optica Publishing Group, in OSA Technical Digest, 2021, p. Th4I.2.
[161] K. Alexander, J. P. George, J. Verbist, et al., "Nanophotonic Pockels modulators on a silicon nitride platform," *Nat. Commun.*, vol. 9, no. 1, p. 3444, 2018.
[162] D. Ban, G. Liu, H. Yu, X. Sun, N. Deng, and F. Qiu, "High electro-optic coefficient lead zirconate titanate films toward low-power and compact modulators," *Opt. Mater. Express*, vol. 11, no. 6, pp. 1733—1741, 2021.
[163] D. Sando, Y. Yang, C. Paillard, B. Dkhil, L. Bellaiche, and V. Nagarajan, "Epitaxial ferroelectric oxide thin films for optical applications," *Appl. Phys. Rev.*, vol. 5, no. 4, p. 041108, 2018.
[164] T. Tan, X. Jiang, C. Wang, B. Yao, and H. Zhang, "2D material optoelectronics for information functional device applications: status and challenges," *Adv. Sci.*, vol. 7, no. 11, p. 2000058, 2020.
[165] B. Yao, S. W. Huang, Y. Liu, et al., "Gate-tunable frequency combs in graphene—nitride microresonators," *Nature*, vol. 558, no. 7710, pp. 410—414, 2018.
[166] C. Qin, K. Jia, Q. Li, et al., "Electrically controllable laser frequency combs in graphene-fibre microresonators," *Light Sci. Appl.*, vol. 9, no. 1, p. 185, 2020.
[167] K. S. Novoselov, V. I. Falko, L. Colombo, P. R. Gellert, M. G. Schwab, and K. Kim, "A roadmap for graphene," *Nature*, vol. 490, no. 7419, pp. 192—200, 2012.
[168] B. C. Yao, Y. J. Rao, S. W. Huang, et al., "Graphene Q-switched distributed feedback fiber lasers with narrow linewidth approaching the transform limit," *Opt. Express*, vol. 25, no. 7, pp. 8202—8211, 2017.
[169] B. C. Yao, Y. J. Rao, Z. N. Wang, et al., "Graphene based widely-tunable and singly-polarized pulse generation with random fiber lasers," *Sci. Rep.*, vol. 5, no. 1, p. 18526, 2015.
[170] X. Jiang, S. Gross, M. J. Withford, et al., "Low-dimensional nanomaterial saturable absorbers for ultrashort-pulsed waveguide lasers," *Opt. Mater. Express*, vol. 8, no. 10, pp. 3055—3071, 2018.
[171] G. Bharathan, L. Xu, X. Jiang, et al., "MXene and PtSe2 saturable absorbers for all-fibre ultrafast mid-infrared lasers," *Opt. Mater. Express*, vol. 11, no. 7, pp. 1898—1906, 2021.
[172] S. Wu, S. Buckley, J. R. Schaibley, et al., "Monolayer semiconductor nanocavity lasers with ultralow thresholds," *Nature*, vol. 520, no. 7545, pp. 69—72, 2015.
[173] T. Ren, P. Song, J. Chen, and K. P. Loh, "Whisper gallery modes in monolayer tungsten disulfide-hexagonal boron nitride optical cavity," *ACS Photonics*, vol. 5, no. 2, pp. 353—358, 2018.

[174] H. Fang, J. Liu, H. Li, et al., "1305 nm few-layer $MoTe_2$-on-Silicon laser-like emission," *Laser Photon. Rev.*, vol. 12, no. 6, p. 1800015, 2018.
[175] Y. Liu, H. Fang, A. Rasmita, et al., "Room temperature nanocavity laser with interlayer excitons in 2D heterostructures," *Sci. Adv.*, vol. 5, no. 4, p. eaav4506, 2019.
[176] Z. Sun, A. Martinez, and F. Wang, "Optical modulators with 2D layered materials," *Nat. Photonics*, vol. 10, p. 227, 2016.
[177] C. T. Phare, Y. H. Daniel Lee, J. Cardenas, and M. Lipson, "Graphene electro-optic modulator with 30 GHz bandwidth," *Nat. Photonics*, vol. 9, no. 8, pp. 511—514, 2015.
[178] S. Yang, D. C. Liu, Z. L. Tan, K. Liu, Z. H. Zhu, and S. Q. Qin, "CMOS-compatible WS2-based all-optical modulator," *ACS Photonics*, vol. 5, no. 2, pp. 342—346, 2018.
[179] R. Peng, K. Khaliji, N. Youngblood, R. Grassi, T. Low, and M. Li, "Midinfrared electro-optic modulation in few-layer black phosphorus," *Nano Lett.*, vol. 17, no. 10, pp. 6315—6320, 2017.
[180] Q. Wu, S. Chen, Y. Wang, et al., "MZI-based all-optical modulator using MXene $Ti_3C_2T_x$ (T = F, O, or OH) deposited microfiber," *Adv. Mater. Technol.*, vol. 4, no. 4, p. 1800532, 2019.
[181] F. Xia, T. Mueller, Y. M. Lin, A. Valdes-Garcia, and P. Avouris, "Ultrafast graphene photodetector," *Nat. Nanotechnol.*, vol. 4, pp. 839—843, 2009.
[182] Q. Qiu and Z. Huang, "Photodetectors of 2D materials from ultraviolet to terahertz waves," *Adv. Mater.*, vol. 33, pp. 2008126-1—2008126-19, 2021.
[183] F. H. L. Koppens, T. Mueller, P. Avouris, A. C. Ferrari, M. S. Vitiello, and M. Polini, "Photodetectors based on graphene, other two-dimensional materials and hybrid systems," *Nat. Nanotechnol.*, vol. 9, no. 10, pp. 780—793, 2014.
[184] Q. Guo, R. Yu, C. Li, et al., "Efficient electrical detection of mid-infrared graphene plasmons at room temperature," *Nat. Mater.*, vol. 17, no. 11, pp. 986—992, 2018.
[185] Q. Liang, Q. Wang, Q. Zhang, et al., "High-performance, room temperature, ultra-broadband photodetectors based on air-stable $PdSe_2$," *Adv. Mater.*, vol. 31, no. 24, p. 1807609, 2019.
[186] P. Wu, L. Ye, L. Tong, et al., "Van der Waals two-color infrared photodetector," *Light Sci. Appl.*, vol. 11, no. 1, p. 6, 2022.
[187] B. Yao, Y. Liu, S. W. Huang, et al., "Broadband gate-tunable terahertz plasmons in graphene heterostructures," *Nat. Photonics*, vol. 12, no. 1, pp. 22—28, 2018.
[188] Y. Li, N. An, Z. Lu, et al., "Nonlinear co-generation of graphene plasmons for optoelectronic logic operations," *Nat. Commun.*, vol. 13, no. 1, p. 3138, 2022.
[189] N. An, T. Tan, Z. Peng, et al., "Electrically tunable four-wave-mixing in graphene heterogeneous fiber for individual gas molecule detection," *Nano Lett.*, vol. 20, no. 9, pp. 6473—6480, 2020.
[190] J. He, I. Paradisanos, T. Liu, et al., "Low-loss integrated nanophotonic circuits with layered semiconductor materials," *Nano Lett.*, vol. 21, pp. 2709—2718, 2021.
[191] R. Wu, J. Zhang, N. Yao, et al., "Lithium niobate micro-disk resonators of quality factors above 10^7," *Opt. Lett.*, vol. 43, pp. 4116—4119, 2018.
[192] Y. Hida, Y. Hibino, H. Okazaki, and Y. Ohmori, "10 m long silica-based waveguide with a loss of 1.7 dB/m," in *Integrated Photonics Research*, vol. 7, Dana Point, California, Optica Publishing Group, in 1995 OSA Technical Digest Series, 1995, p. IThC6.
[193] K. Y. Yang, D. Y. Oh, S. H. Lee, et al., "Bridging ultrahigh-Q devices and photonic circuits," *Nat. Photonics*, vol. 12, no. 5, pp. 297—302, 2018.
[194] N. Hattasan, B. Kuyken, F. Leo, E. M. P. Ryckeboer, D. Vermeulen, and G. Roelkens, "High-efficiency SOI fiber-to-chip grating couplers and low-loss waveguides for the short-wave infrared," *IEEE Photon. Technol. Lett.*, vol. 24, no. 17, pp. 1536—1538, 2012.
[195] G. Z. Mashanovich, M. M. Milosevic, M. Nedeljkovic, et al., "Low loss silicon waveguides for the mid-infrared," *Opt. Express*, vol. 19, no. 8, pp. 7112—7119, 2011.
[196] J. Soler Penades, A. Z. Khokhar, M. Nedeljkovic, and G. Z. Mashanovich, "Low-loss mid-infrared SOI slot waveguides," *IEEE Photon. Technol. Lett.*, vol. 27, no. 11, pp. 1197—1199, 2015.
[197] M. Nedeljkovic, A. Z. Khokhar, Y. Hu, et al., "Silicon photonic devices and platforms for the mid-infrared," *Opt. Mater. Express*, vol. 3, no. 9, pp. 1205—1214, 2013.
[198] C. Bellegarde, E. Pargon, C. Sciancalepore, et al., "Improvement of sidewall roughness of submicron SOI waveguides by hydrogen plasma and annealing," *IEEE Photon. Technol. Lett.*, vol. 30, no. 7, pp. 591—594, 2018.
[199] T. Horikawa, D. Shimura, and T. Mogami, "Low-loss silicon wire waveguides for optical integrated circuits," *MRS Commun.*, vol. 6, no. 1, pp. 9—15, 2016.
[200] A. Biberman, M. J. Shaw, E. Timurdogan, J. B. Wright, and M. R. Watts, "Ultralow-loss silicon ring resonators," *Opt. Lett.*, vol. 37, no. 20, pp. 4236—4238, 2012.
[201] L. Zhang, L. Jie, M. Zhang, et al., "Ultrahigh-Q silicon racetrack resonators," *Photonics Res.*, vol. 8, no. 5, pp. 684—689, 2020.
[202] L. Zhang, S. Hong, Y. Wang, et al., "Ultralow-loss silicon photonics beyond the singlemode regime," *Laser Photon. Rev.*, vol. 16, no. 4, p. 2100292, 2022.
[203] T. J. Morin, L. Chang, W. Jin, et al., "CMOS-foundry-based blue and violet photonics," *Optica*, vol. 8, no. 5, pp. 755—756, 2021.
[204] C. Sorace-Agaskar, S. Bramhavar, D. Kharas, et al., *Multi-layer Integrated Photonics from the Ultraviolet to the Infrared (SPIE BiOS)*, San Francisco, California, SPIE, 2018.
[205] N. Chauhan, J. Wang, D. Bose, et al., "Ultra-low loss visible light waveguides for integrated atomic, molecular, and quantum photonics," *Opt. Express*, vol. 30, no. 5, pp. 6960—6969, 2022.
[206] P. T. Lin, V. Singh, H. Y. G. Lin, T. Tiwald, L. C. Kimerling, and A. M. Agarwal, "Low-stress silicon nitride platform for mid-infrared broadband and monolithically integrated microphotonics," *Adv. Opt. Mater.*, vol. 1, no. 10, pp. 732—739, 2013.
[207] K. Luke, Y. Okawachi, M. R. E. Lamont, A. L. Gaeta, and M. Lipson, "Broadband mid-infrared frequency comb generation in a Si_3N_4 microresonator," *Opt. Lett.*, vol. 40, no. 21, pp. 4823—4826, 2015.
[208] P. Tai Lin, V. Singh, L. Kimerling, and A. M. Agarwal, "Planar silicon nitride mid-infrared devices," *Appl. Phys. Lett.*, vol. 102, no. 25, p. 251121, 2013.
[209] M. W. Puckett, K. Liu, N. Chauhan, et al., "422 Million intrinsic quality factor planar integrated all-waveguide resonator with sub-MHz linewidth," *Nat. Commun.*, vol. 12, no. 1, p. 934, 2021.
[210] X. Ji, X. Yao, Y. Gan, et al., "On-chip tunable photonic delay line," *APL Photonics*, vol. 4, no. 9, p. 090803, 2019.
[211] W. Jin, Q. F. Yang, L. Chang, et al., "Hertz-linewidth semiconductor lasers using CMOS-ready ultra-high-Q microresonators," *Nat. Photonics*, vol. 15, no. 5, pp. 346—353, 2021.

[212] X. Liu, A. W. Bruch, Z. Gong, et al., "Ultra-high-Q UV microring resonators based on a single-crystalline AlN platform," *Optica*, vol. 5, no. 10, pp. 1279—1282, 2018.
[213] J. Liu, X. Ma, S. Wang, et al., "High Q AlN ring cavity with wet chemical etching for post-treatment," in *Asia Communications and Photonics Conference (ACPC) 2019*, Chengdu, Optica Publishing Group, in OSA Technical Digest, 2019, p. M4A.236.
[214] G. N. West, W. Loh, D. Kharas, et al., "Low-loss integrated photonics for the blue and ultraviolet regime," *APL Photonics*, vol. 4, no. 2, p. 026101, 2019.
[215] J. Zhang, Z. Fang, J. Lin, et al., "Fabrication of crystalline microresonators of high quality factors with a controllable wedge angle on lithium niobate on insulator," *Nanomaterials*, vol. 9, no. 9, pp. 1—7, 2019.
[216] R. Soref and J. Larenzo, "All-silicon active and passive guided-wave components for $\lambda = 1.3$ and 1.6 μm," *IEEE J. Quantum Electron.*, vol. 22, no. 6, pp. 873—879, 1986.
[217] R. Soref, "The past, present, and future of silicon photonics," *IEEE J. Sel. Top. Quantum Electron.*, vol. 12, no. 6, pp. 1678—1687, 2006.
[218] D. Liang, G. Roelkens, R. Baets, and J. Bowers, "Hybrid integrated platforms for silicon photonics," *Materials*, vol. 3, no. 3, p. 1782, 2010.
[219] B. Sepúlveda, J. S. d. Rio, M. Moreno, et al., "Optical biosensor microsystems based on the integration of highly sensitive Mach—Zehnder interferometer devices," *J. Opt. A Pure Appl. Opt.*, vol. 8, no. 7, pp. S561—S566, 2006.
[220] F. T. Dullo, S. Lindecrantz, J. Jagerska, et al., "Sensitive on-chip methane detection with a cryptophane-A cladded Mach—Zehnder interferometer," *Opt. Express*, vol. 23, no. 24, pp. 31564—31573, 2015.
[221] A. B. González-Guerrero, M. Alvarez, A. G. Castaño, C. Domínguez, and L. M. Lechuga, "A comparative study of in-flow and micro-patterning biofunctionalization protocols for nanophotonic silicon-based biosensors," *J. Colloid Interface Sci.*, vol. 393, pp. 402—410, 2013.
[222] D. Zecca, A. Qualtieri, G. Magno, et al., "Label-free Si_3N_4 photonic crystal based immunosensors for diagnostic applications," *IEEE Photon. J.*, vol. 6, no. 6, pp. 1—7, 2014.
[223] R. Diekmann, O. I. Helle, C. I. Oie, et al., "Chip-based wide field-of-view nanoscopy," *Nat. Photonics*, vol. 11, no. 5, pp. 322—328, 2017.
[224] A. T. Mashayekh, T. Klos, D. Geuzebroek, et al., "Silicon nitride PIC-based multi-color laser engines for life science applications," *Opt. Express*, vol. 29, no. 6, pp. 8635—8653, 2021.
[225] X. Ji, D. Mojahed, Y. Okawachi, A. L. Gaeta, C. P. Hendon, and M. Lipson, "Millimeter-scale chip—based supercontinuum generation for optical coherence tomography," *Sci. Adv.*, vol. 7, no. 38, p. eabg8869, 2021.
[226] M. S. Eggleston, F. Pardo, C. Bolle, et al., "Sensitivity in a chip-scale swept-source optical coherence tomography system," in *CLEO: Science and Innovations*, Optical Society of America, 2018, p. JTh5C.8.
[227] K. D. Hakkel, M. Petruzzella, F. Ou, et al., "Integrated near-infrared spectral sensing," *Nat. Commun.*, vol. 13, no. 1, p. 103, 2022.
[228] P. T. Lin, V. Singh, Y. Cai, L. C. Kimerling, and A. Agarwal, "Air-clad silicon pedestal structures for broadband mid-infrared microphotonics," *Opt. Lett.*, vol. 38, no. 7, pp. 1031—1033, 2013.
[229] J. S. Penadés, C. Alonso-Ramos, A. Z. Khokhar, et al., "Suspended SOI waveguide with sub-wavelength grating cladding for mid-infrared," *Opt. Lett.*, vol. 39, no. 19, pp. 5661—5664, 2014.
[230] Y. Xia, C. Qiu, X. Zhang, W. Gao, J. Shu, and Q. Xu, "Suspended Si ring resonator for mid-IR application," *Opt. Lett.*, vol. 38, no. 7, pp. 1122—1124, 2013.
[231] J. Chiles, S. Khan, J. Ma, and S. Fathpour, "High-contrast, all-silicon waveguiding platform for ultra-broadband mid-infrared photonics," *Appl. Phys. Lett.*, vol. 103, no. 15, p. 151106, 2013.
[232] C. Ranacher, C. Consani, A. Tortschanoff, et al., "Mid-infrared absorption gas sensing using a silicon strip waveguide," *Sens. Actuators A Phys.*, vol. 277, pp. 117—123, 2018.
[233] W. Liu, Y. Ma, Y. Chang, et al., "Suspended silicon waveguide platform with subwavelength grating metamaterial cladding for long-wave infrared sensing applications," *Nanophotonics*, vol. 10, no. 7, pp. 1861—1870, 2021.
[234] Yariv Group, *On-Chip Label-Free Optical Bio-Sensing Using Monolithic Optical Micro-Resonators*, 2022. Available at: http://www.its.caltech.edu/∼aphyariv/research.html.
[235] S. A. Diddams, K. Vahala, and T. Udem, "Optical frequency combs: coherently uniting the electromagnetic spectrum," *Science*, vol. 369, no. 6501, p. eaay3676, 2020.
[236] H. A. Haus, "Mode-locking of lasers," *IEEE J. Sel. Top. Quantum Electron.*, vol. 6, no. 6, pp. 1173—1185, 2000.
[237] P. Del'Haye, A. Schliesser, O. Arcizet, T. Wilken, R. Holzwarth, and T. J. Kippenberg, "Optical frequency comb generation from a monolithic microresonator," *Nature*, vol. 450, no. 7173, pp. 1214—1217, 2007.
[238] E. Obrzud, S. Lecomte, and T. Herr, "Temporal solitons in microresonators driven by optical pulses," *Nat. Photonics*, vol. 11, no. 9, pp. 600—607, 2017.
[239] A. A. Savchenkov, A. B. Matsko, V. S. Ilchenko, I. Solomatine, D. Seidel, and L. Maleki, "Tunable optical frequency comb with a crystalline whispering gallery mode resonator," *Phys. Rev. Lett.*, vol. 101, no. 9, p. 093902, 2008.
[240] Y. Okawachi, K. Saha, J. S. Levy, Y. H. Wen, M. Lipson, and A. L. Gaeta, "Octave-spanning frequency comb generation in a silicon nitride chip," *Opt. Lett.*, vol. 36, no. 17, pp. 3398—3400, 2011.
[241] M. A. Foster, J. S. Levy, O. Kuzucu, K. Saha, M. Lipson, and A. L. Gaeta, "Silicon-based monolithic optical frequency comb source," *Opt. Express*, vol. 19, no. 15, pp. 14233—14239, 2011.
[242] M. Peccianti, A. Pasquazi, Y. Park, et al., "Demonstration of a stable ultrafast laser based on a nonlinear microcavity," *Nat. Commun.*, vol. 3, no. 1, p. 765, 2012.
[243] F. Ferdous, H. Miao, P. H. Wang, et al., "Probing coherence in microcavity frequency combs via optical pulse shaping," *Opt. Express*, vol. 20, no. 19, pp. 21033—21043, 2012.
[244] W. Liang, A. A. Savchenkov, Z. Xie, et al., "Miniature multioctave light source based on a monolithic microcavity," *Optica*, vol. 2, no. 1, pp. 40—47, 2015.
[245] H. Zhou, Y. Geng, W. Cui, et al., "Soliton bursts and deterministic dissipative Kerr soliton generation in auxiliary-assisted microcavities," *Light Sci. Appl.*, vol. 8, no. 1, p. 50, 2019.
[246] J. Yang, S. W. Huang, Z. Xie, M. Yu, D. L. Kwong, and C. W. Wong, "Coherent satellites in multispectral regenerative frequency microcombs," *Commun. Phys.*, vol. 3, no. 1, p. 27, 2020.

[247] Y. S. Jang, H. Liu, J. Yang, M. Yu, D. L. Kwong, and C. W. Wong, "Nanometric precision distance metrology via hybrid spectrally resolved and homodyne interferometry in a single soliton frequency microcomb," *Phys. Rev. Lett.*, vol. 126, no. 2, p. 023903, 2021.
[248] A. Vakil and N. Engheta, "Transformation optics using graphene," *Science*, vol. 332, no. 6035, pp. 1291–1294, 2011.
[249] T. Gu, N. Petrone, J. F. McMillan, et al., "Regenerative oscillation and four-wave mixing in graphene optoelectronics," *Nat. Photonics*, vol. 6, no. 8, pp. 554–559, 2012.
[250] H. Zhou, X. Zhu, T. Gu, et al., "Error-free data transmission through fast broadband all-optical modulation in graphene–silicon optoelectronics," *Appl. Phys. Lett.*, vol. 116, no. 22, p. 221106, 2020.
[251] V. S. Ilchenko, A. A. Savchenkov, A. B. Matsko, and L. Maleki, "Dispersion compensation in whispering-gallery modes," *J. Opt. Soc. Am. A*, vol. 20, no. 1, pp. 157–162, 2003.
[252] C. J. Chen, C. A. Husko, I. Meric, et al., "Deterministic tuning of slow-light in photonic-crystal waveguides through the C and L bands by atomic layer deposition," *Appl. Phys. Lett.*, vol. 96, no. 8, p. 081107, 2010.
[253] A. B. Matsko, A. A. Savchenkov, and L. Maleki, "Normal group-velocity dispersion Kerr frequency comb," *Opt. Lett.*, vol. 37, no. 1, pp. 43–45, 2012.
[254] S. W. Huang, J. Yang, M. Yu, et al., "A broadband chip-scale optical frequency synthesizer at 2.7×10^{-16} relative uncertainty," *Sci. Adv.*, vol. 2, no. 4, p. e1501489, 2016.
[255] C. Godey, I. V. Balakireva, A. Coillet, and Y. K. Chembo, "Stability analysis of the spatiotemporal Lugiato–Lefever model for Kerr optical frequency combs in the anomalous and normal dispersion regimes," *Phys. Rev. A*, vol. 89, no. 6, p. 063814, 2014.
[256] S. W. Huang, H. Zhou, J. Yang, et al., "Mode-locked ultrashort pulse generation from on-chip normal dispersion microresonators," *Phys. Rev. Lett.*, vol. 114, no. 5, p. 053901, 2015.
[257] S. W. Huang, H. Liu, J. Yang, M. Yu, D. L. Kwong, and C. W. Wong, "Smooth and flat phase-locked Kerr frequency comb generation by higher order mode suppression," *Sci. Rep.*, vol. 6, no. 1, p. 26255, 2016.
[258] S. W. Huang, J. Yang, S. H. Yang, et al., "Globally stable microresonator turing pattern formation for coherent high-power THz radiation on-chip," *Phys. Rev. X*, vol. 7, pp. 041002-1–041002-10, 2017.
[259] Y. Li, S. W. Huang, B. Li, et al., "Real-time transition dynamics and stability of chip-scale dispersion-managed frequency microcombs," *Light Sci. Appl.*, vol. 9, no. 1, p. 52, 2020.
[260] W. Wang, H. Liu, J. Yang, A. K. Vinod, and C. W. Wong, "Mapping ultrafast timing jitter in dispersion-managed 89 GHz frequency microcombs via self-heterodyne linear interferometry," arXiv:2108.01177, 2021.
[261] H. J. C. Teng Tan, Z. Yuan, Y. Yu, Q. T. Cao, "Gain-assisted chiral soliton microcombs," arXiv:2008.12510, 2020.
[262] C. Xiang, J. Liu, J. Guo, et al., "Laser soliton microcombs heterogeneously integrated on silicon," *Science*, vol. 373, no. 6550, pp. 99–103, 2021.
[263] L. Chang, S. Liu, and J. E. Bowers, "Integrated optical frequency comb technologies," *Nat. Photonics*, vol. 16, no. 2, pp. 95–108, 2022.
[264] A. L. Gaeta, M. Lipson, and T. J. Kippenberg, "Photonic-chip-based frequency combs," *Nat. Photonics*, vol. 13, no. 3, pp. 158–169, 2019.
[265] H. J. Chen, Q. X. Ji, H. Wang, et al., "Chaos-assisted two-octave-spanning microcombs," *Nat. Commun.*, vol. 11, no. 1, p. 2336, 2020.
[266] Q. F. Yang, Q. X. Ji, L. Wu, et al., "Dispersive-wave induced noise limits in miniature soliton microwave sources," *Nat. Commun.*, vol. 12, no. 1, p. 1442, 2021.
[267] X. Wang, P. Xie, W. Wang, et al., "Program-controlled single soliton microcomb source," *Photonics Res.*, vol. 9, no. 1, pp. 66–72, 2021.
[268] Z. Lu, H. J. Chen, W. Wang, et al., "Synthesized soliton crystals," *Nat. Commun.*, vol. 12, no. 1, p. 3179, 2021.
[269] C. Wang, Z. Fang, A. Yi, et al., "High-Q microresonators on 4H-silicon-carbide-on-insulator platform for nonlinear photonics," *Light Sci. Appl.*, vol. 10, no. 1, p. 139, 2021.
[270] X. Liu, C. Sun, B. Xiong, et al., "Generation of multiple near-visible comb lines in an AlN microring via $\chi^{(2)}$ and $\chi^{(3)}$ optical nonlinearities," *Appl. Phys. Lett.*, vol. 113, no. 17, p. 171106, 2018.
[271] S. Miller, K. Luke, Y. Okawachi, J. Cardenas, A. L. Gaeta, and M. Lipson, "On-chip frequency comb generation at visible wavelengths via simultaneous second- and third-order optical nonlinearities," *Opt. Express*, vol. 22, no. 22, pp. 26517–26525, 2014.
[272] Y. Zhao, X. Ji, B. Y. Kim, et al., "Visible nonlinear photonics via high-order-mode dispersion engineering," *Optica*, vol. 7, no. 2, pp. 135–141, 2020.
[273] A. K. Vinod, S. W. Huang, J. Yang, M. Yu, D. L. Kwong, and C. W. Wong, "Frequency microcomb stabilization via dual-microwave control," *Commun. Phys.*, vol. 4, pp. 1–10, 2021.
[274] Y. Geng, H. Zhou, X. Han, et al., "Coherent optical communications using coherence-cloned Kerr soliton microcombs," *Nat. Commun.*, vol. 13, no. 1, p. 1070, 2022.
[275] N. Gisin and R. Thew, "Quantum communication," *Nat. Photonics*, vol. 1, no. 3, pp. 165–171, 2007.
[276] H. K. Lo, M. Curty, and K. Tamaki, "Secure quantum key distribution," *Nat. Photonics*, vol. 8, no. 8, pp. 595–604, 2014.
[277] P. Kok, W. J. Munro, K. Nemoto, T. C. Ralph, J. P. Dowling, and G. J. Milburn, "Linear optical quantum computing with photonic qubits," *Rev. Mod. Phys.*, vol. 79, no. 1, pp. 135–174, 2007.
[278] V. Giovannetti, S. Lloyd, and L. Maccone, "Advances in quantum metrology," *Nat. Photonics*, vol. 5, no. 4, pp. 222–229, 2011.
[279] C. D. Bruzewicz, J. Chiaverini, R. McConnell, and J. M. Sage, "Trapped-ion quantum computing: progress and challenges," *Appl. Phys. Rev.*, vol. 6, no. 2, p. 021314, 2019.
[280] C. Simon, M. Afzelius, J. Appel, et al., "Quantum memories," *Eur. Phys. J. D*, vol. 58, no. 1, pp. 1–22, 2010.
[281] K. R. Brown, J. Chiaverini, J. M. Sage, and H. Häffner, "Materials challenges for trapped-ion quantum computers," *Nat. Rev. Mater.*, vol. 6, no. 10, pp. 892–905, 2021.
[282] K. K. Mehta, C. D. Bruzewicz, R. McConnell, R. J. Ram, J. M. Sage, and J. Chiaverini, "Integrated optical addressing of an ion qubit," *Nat. Nanotechnol.*, vol. 11, no. 12, pp. 1066–1070, 2016.

[283] L. Caspani, C. Xiong, B. J. Eggleton, et al., "Integrated sources of photon quantum states based on nonlinear optics," *Light Sci. Appl.*, vol. 6, no. 11, pp. e17100, 2017.
[284] X. Lu, Q. Li, D. A. Westly, et al., "Chip-integrated visible–telecom entangled photon pair source for quantum communication," *Nat. Phys.*, vol. 15, no. 4, pp. 373–381, 2019.
[285] E. A. Swanson, *Optical Coherence Tomography — Principles and Applications*, San Francisco, California, IEEE, 2003.
[286] X. Guo, A. He, and Y. Su, "Recent advances of heterogeneously integrated III–V laser on Si," *J. Semiconduct.*, vol. 40, no. 10, p. 101304, 2019.
[287] Z. Zhou, B. Yin, and J. Michel, "On-chip light sources for silicon photonics," *Light Sci. Appl.*, vol. 4, p. e358, 2015.
[288] I. A. Fischer, M. Brehm, M. De Seta, et al., "On-chip infrared photonics with Si-Ge-heterostructures: what is next?" *APL Photonics*, vol. 7, no. 5, p. 050901, 2022.